AFRL-AFOSR-VA-TR-2020-0135

Developing a Hybrid SThM-SEM System with High Spatiotemporal Resolutin for Transient Thermal Characterization of Electronic Materials and Devices

Yanbao Ma
UNIVERSITY OF CALIFORNIA MERCED

08/15/2020
Final Report

DISTRIBUTION A: Distribution approved for public release.

Air Force Research Laboratory
AF Office Of Scientific Research (AFOSR)/ RTB2
Arlington, Virginia 22203
Air Force Materiel Command

REPORT DOCUMENTATION PAGE

Form Approved
OMB No. 0704-0188

The public reporting burden for this collection of information is estimated to average 1 hour per response, including the time for reviewing instructions, searching existing data sources, gathering and maintaining the data needed, and completing and reviewing the collection of information. Send comments regarding this burden estimate or any other aspect of this collection of information, including suggestions for reducing the burden, to Department of Defense, Executive Services, Directorate (0704-0188). Respondents should be aware that notwithstanding any other provision of law, no person shall be subject to any penalty for failing to comply with a collection of information if it does not display a currently valid OMB control number.
PLEASE DO NOT RETURN YOUR FORM TO THE ABOVE ORGANIZATION.

1. REPORT DATE *(DD-MM-YYYY)* 15-08-2020	**2. REPORT TYPE** Final Performance	**3. DATES COVERED** *(From - To)* 01 Apr 2018 to 31 Mar 2020

4. TITLE AND SUBTITLE
Developing a Hybrid SThM-SEM System with High Spatiotemporal Resolutin for Transient Thermal Characterization of Electronic Materials and Devices

5a. CONTRACT NUMBER

5b. GRANT NUMBER
FA9550-18-1-0086

5c. PROGRAM ELEMENT NUMBER
61102F

6. AUTHOR(S)
Yanbao Ma

5d. PROJECT NUMBER

5e. TASK NUMBER

5f. WORK UNIT NUMBER

7. PERFORMING ORGANIZATION NAME(S) AND ADDRESS(ES)
UNIVERSITY OF CALIFORNIA MERCED
5200 N LAKE RD
MERCED, CA 95343-5001 US

8. PERFORMING ORGANIZATION REPORT NUMBER

9. SPONSORING/MONITORING AGENCY NAME(S) AND ADDRESS(ES)
AF Office of Scientific Research
875 N. Randolph St. Room 3112
Arlington, VA 22203

10. SPONSOR/MONITOR'S ACRONYM(S)
AFRL/AFOSR RTB2

11. SPONSOR/MONITOR'S REPORT NUMBER(S)
AFRL-AFOSR-VA-TR-2020-0135

12. DISTRIBUTION/AVAILABILITY STATEMENT
A DISTRIBUTION UNLIMITED: PB Public Release

13. SUPPLEMENTARY NOTES

14. ABSTRACT

The electron beam (e-beam) in the scanning electron microscopy (SEM) provides an appealing mobile heating source for thermal metrology with spatial resolution of ~ 1 nm, but the lack of systematic quantification of the e-beam heating power limits such application development. We demonstrated the capability of using e-beam (SEM) as a quantitative heating source from both experimental and theoretical approaches, and further e-beam based thermal conductivity measurement promotes this heating source characterization. This provides a foundation to adopt e-beam to develop high resolution thermal probing techniques in SEM in addition to its high- resolution imaging capability.

15. SUBJECT TERMS
thermal transport, nanoscale, scanning microscopy, numerical analysis

16. SECURITY CLASSIFICATION OF:			**17. LIMITATION OF ABSTRACT**	**18. NUMBER OF PAGES**	**19a. NAME OF RESPONSIBLE PERSON**
a. REPORT	**b. ABSTRACT**	**c. THIS PAGE**			GORETTA, KENNETH
Unclassified	Unclassified	Unclassified	UU		**19b. TELEPHONE NUMBER** *(Include area code)* 703-696-7349

Standard Form 298 (Rev. 8/98)
Prescribed by ANSI Std. Z39.18

DISTRIBUTION A: Distribution approved for public release.

Development of electron beam based thermal probing technique in micro- and nanoscale

FA9550-18-1-0086

Yanbao Ma

Department of Mechanical Engineering

University of California at Merced

Contents

DISTRIBUTION A: Distribution approved for public release.

1. Summary

The electron beam (e-beam) in the scanning electron microscopy (SEM) provides an appealing mobile heating source for thermal metrology with spatial resolution of ~ 1 nm, but the lack of systematic quantification of the e-beam heating power limits such application development. Here, we systemically study e-beam heating in LPCVD silicon nitride (SiN*x*) thin-films with thickness ranging from 200 to 500 nm from both experiments and complementary Monte Carlo simulations using the CASINO software. There is good agreement about the thickness-dependent e-beam energy absorption of thin-film between modeling predictions and experiments. Using the absorption results we then demonstrate adapting e-beam as a quantitative heat source by measuring the thickness-dependent thermal conductivity of SiN*x* thin-films, with the results validated to within 7% by a separate Joule heating experiment. The results described here will open a new avenue to using SEM e-beams as a mobile heating source for advanced nanoscale thermal metrology development.

We demonstrated the capability of using e-beam (SEM) as a quantitative heating source from both experimental and theoretical approaches, and further e-beam based thermal conductivity measurement promotes this heating source characterization. This provides a foundation to adopt e-beam to develop high resolution thermal probing techniques in SEM in addition to its high-resolution imaging capability.

DISTRIBUTION A: Distribution approved for public release.

2. Introduction

The interaction between the high-kinetic energy electrons from an electron beam (e-beam) and a sample produces a wealth of signals which provide a variety of insights for scanning electron microscopy (SEM), such as analyzing composition, imaging surface morphology, and investigating the crystalline structures. During the electron-substrate interaction, heat is also generated and this makes it possible to apply the e-beam as a high-quality mobile heat source for generating nanoscale thermal hotspots, but also for thermal studies in SEM and TEM [1-6].

E-beams have several unique characteristics which are appealing for nanoscale thermal metrology. First, an e-beam's potential spatial resolution of ~1 nm is appealing compared to that of alternate techniques for nanoscale thermal measurements, such as the 3ω method, time/frequency-domain thermoreflectance, and Raman/luminescence-based methods, which are generally limited by the microfabrication length scale or optical diffraction limit [7-9]. Similarly, focusing a high-energy e-beam into such a small area results in nanoscale heat sources with extraordinarily high heat fluxes, easily exceeding ~1 $\mathrm{MWcm^{-2}}$. This is valuable for the study of heat dissipation from nanoscale hotspots, which is important for both fundamental understanding and engineering design in micro- and nano-electronics, because nanometer-scale hotspots of up to hundreds of degrees Celsius are believed to influence device performance and reliability[10]. Furthermore, compared to Joule heating by microfabricated heater lines or scanning with a heated atomic force microscope tip [11, 12], the e-beam's dynamically-controllable shape and position makes it a more nimble heat source for precise manufacturing and thermal studies.

Understanding e-beam heating is also important for one of the most widespread applications of e-beams, namely imaging in scanning- and transmission-electron microscopies (SEM and TEM), in which this heating is a critical factor limiting the acquisition of structural or chemical data at high spatial resolution [13, 14], especially for imaging with high e-beam energy in TEM [15, 16] and imaging low thermal conductivity materials in SEM [1, 17]. Similarly, in e-beam lithography temperature effects on the e-beam resist are a significant contributor to errors in feature size and pattern placement[18]. However, the characterization and quantification of nanoscale e-beam heating is still a topic that has seen little research, especially experimentally.

For imaging, the interactions between the incident e-beam and the target materials are routinely simulated using Monte Carlo (MC) techniques[19]. Especially, the CASINO software package [20-22] is widely used to simulate the electron-substrate interactions in SEM, and has also been applied to develop metrology to estimate thin film thickness based on the intensities of backscattered and secondary electron signals [23, 24]. However, the resultant heating phenomena have rarely been considered. One notable example combined MC simulation of the e-beam energy deposition with electron and phonon hydrodynamic transport equations in the substrate, though such calculations have not yet been experimentally validated [25, 26]. Indeed, to the best of our knowledge the e-beam energy deposition in thin films as predicted by CASINO has never been experimentally verified.

Early experimental studies of e-beam heating included using thin film thermocouples to measure heating during e-beam lithography [27, 28] and the temperature rise of e-beam irradiated freestanding thin films [29, 30]. The thin film studies observed a strong and non-monotonic dependence of the temperature rise on the e-beam voltage [30], the physics of which was not understood but will be explained in detail below. More recently, e-beam heating in SEM/TEM has been applied for thermal measurements to demonstrate a new micro-thermometer based on vanadium dioxide nanowire [1], and to measure the spatially resolved thermal conductance of nanowires [2, 3] and two-dimensional materials (graphene [31], black phosphorus [32], and MoS_2 [33]). However, in all of these previous studies, the quantitative power delivered by the e-beam was not used (refs 27-30) or canceled out (refs 1-3) of the final thermal measurement. Therefore, the e-beam has not yet been used as a quantitative heat source for thermal measurement.

In this report, we have studied the e-beam heating of suspended silicon nitride (SiN_x) thin films with thickness ranging from 200 to 500 nm using micro-fabricated calorimeter devices inside a standard SEM. The results validate the absorption energy profiles calculated by CASINO. Then, for the first time, we adapt the e-beam as a quantitative heat source to measure the in-plane thermal conductivity of SiN_x thin films, with results in good agreement with independent measurements using a Joule heating method. These results will help develop the application of e-beam as an advanced mobile heating source for future thermal metrologies at the micro and nanoscale.

Besides, we show several ideas to potentially apply e-beam with modulation for advanced applications.

3. Major results

DISTRIBUTION A: Distribution approved for public release.

A. Adapting the electron beam from SEM as a quantitative steady-state heating source for nanoscale thermal metrology

a. Theoretical energy absorption study of the electron beam in SiN*x* thin film

As an electron beam interacts with a specimen, the beam undergoes numerous elastic and inelastic scattering events. Besides creating a broad range of signals can be used for material analysis, here the inelastic interactions are the main focus because they convert energy from the primary e-beam into heat in the specimen. To obtain a statistical understanding of these complex interactions in the specimen, a MC based electron trajectory simulation can be performed which calculates the paths of numerous incident electrons using random numbers. In this work, we use CASINO v2.5.1.0 (Monte CArlo SImulation of electroN trajectory in sOlids) [20-22] to conduct the MC simulation. Targeting the interaction in SEM, CASINO considers key parameters like the e-beam voltage (the kinetic energy of an incident electron) and the atomic number, thickness, and density of the specimen material. The results are widely accepted for describing the shape and size of the interaction volume, though experimental validation was not previously available regarding the energy deposition.

The CASINO software package calculates the electron trajectories within the specimen using Monte Carlo methods to model the various physical interactions between the electrons and the sample [20]. The program tracks the electron trajectories as dictated by the elastic scattering events (see example in Fig. 1), while the inelastic events between every consecutive pair of elastic scatterings are estimated by the mean energy loss model. The absorbed energy from the e-beam is from the inelastic events, which in CASINO are approximated as being uniformly distributed along the electron's path between consecutive elastic scattering events. A continuous slowing-down equation is used to model this phenomenon (electron energy loss per unit path length), which combined with an estimation of the stopping energy determines the lateral and vertical electron range, and the corresponding spatial distribution of the inelastic energy transfer. In CASINO, several models can be selected for different interaction conditions. We complete the calculation of each electron trajectory by the following steps. First, the initial voltage (various, from 2 kV to 20 kV), direction (normally incident on the sample surface), and diameter (3 nm) of the e-beam is specified. Note that we varied the diameter of e-beam and found that the absorbed energy is insensitive to the diameter varying from 1 nm to 10 nm. For each electron, the distance between

DISTRIBUTION A: Distribution approved for public release.

consecutive elastic collisions is obtained based on the total elastic scattering cross-section, in which a random number is used to distribute the distance following a probability distribution. The elastic scattering angle is then determined from another random number and using the differential cross-section from standardized tabulated values. These steps were then repeated until an electron leaves the sample or is trapped inside the sample based on the stopping energy. Here we use a piecewise model of the energy loss function, which combines one model (ref. [19]) for low e-beam energies (< 10 keV) and the Bethe (1930) equation for high e-beam energies (10 - 30 keV), which together provide a well-accepted and simple analytical expression for the stopping power [34]. The cross-section representing the distance between elastic collisions is computed using the tabulated Mott elastic scattering cross-sections of Czyzewski *et al* [35]. To obtain a sufficiently small statistical error, a total of 50,000 electron trajectories were calculated for each condition. Finally, the cumulative statistics of all 50,000 electron trajectories are used to determine the distribution of absorbed energy throughout the sample and calculate the total absorption fraction.

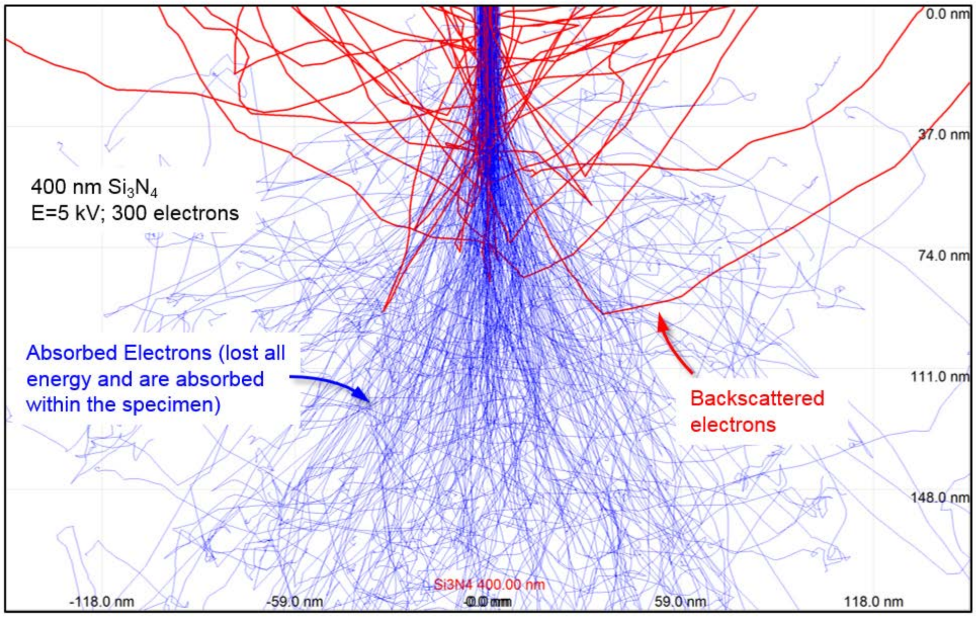

Figure 1. Example of CASINO Monte Carlo electron trajectories for 400 nm thick Si_3N_4 thin film. Here only 300 electron trajectories are shown to make it easier to differentiate the absorbed electrons (blue) and the backscattered electrons (red). Only the top 185 nm of the sample is shown.

In this work, we choose free-standing SiN*x* films as the system for studying e-beam energy absorption because SiN*x* is a well-studied structural dielectric used in many microelectronic and

MEMS devices [36, 37]. To determine the absorbed energy in SiN*x* thin films from CASINO simulations, we need to set the specimen information and the microscope conditions. For the specimen we use three layers, namely a SiN*x* thin film sandwiched by the vacuum. The SiN*x* chemical composition is specified with the atomic fraction x ranging from 1.1 to 1.5 to match the experimental samples as fabricated by LPCVD and detailed in the following sections. The microscope conditions include the electron beam accelerating voltage, the focused beam size, the number of simulated electron trajectories, and the angle between the specimen normal and the beam direction, and are all set in CASINO to match our experimental conditions.

We first consider CASINO simulations of SiN*x* films with thickness t from 200 - 500 nm and incident e-beam voltages E from 2 - 20 kV. Note that the e-beam energy will be directly set in the unit of electronvolt (eV) in the CASINO program, however we will use the accelerating voltage in the unit of volt (V) to quantify the e-beam energy to make direct comparison with following experiment results. As a representative result, Fig. 1a shows the deposited energy distribution inside a 200 nm thick Si_3N_4 (or SiN*x*, $x = 1.33$) thin film for several e-beam voltages. Taking the e-beam voltage of 4 kV for example, the simulation depicts the cross-section of a bulb-shaped electron–matter interaction volume corresponding to the material of low atomic number ($Z = 11.2$ for Si_3N_4, averaged based on weight fraction [22]). Materials of higher atomic number ($Z > 50$) show a more hemispherical shaped interaction volume [38].

For low e-beam voltages when the e-beam penetration depth is smaller than the film thickness, the absorbed energy increases almost linearly with the e-beam voltage as shown in Fig. 2b. This corresponds to a nearly constant fraction of each incident electron's energy being absorbed in the film, defined as the electron energy absorption coefficient α, here around 82% as seen in Fig. 2c at low energies. We define α such that

$$E_{\mathrm{abs}} = \alpha E\,, \tag{1}$$

where E is the energy of the incident e-beam and E_{abs} is the corresponding absorbed energy in the film. Even though at low E there is no electron transmission through the sample, the maximum α remains less than 100% because energy is still lost through secondary electrons, back-scattered electrons, *x*-rays, *etc*.

Then, upon increasing the e-beam voltage beyond some critical value (~ 4 kV for 200 nm thick SiNx), a finite and then increasing fraction of the incident electrons can transmit completely through the film. As a result, α decreases with increasing e-beam voltage. We define the e-beam voltage giving the maximum E_{abs} in Fig. 2b as the "most-efficient-e-beam-heating-voltage" (MEEHV). For this specimen of 200 nm thick SiN_x the MEEHV is 4.63 ± 0.35 kV, where the uncertainty range corresponds to varying x from 1.1 to 1.5. When the actual e-beam voltage is below this MEEHV level, the thin film can still absorb most of the incident electrons ($\alpha \approx$ const.), so E_{abs} will increase in direct proportion to E in accordance with Eq. (1). However, when the e-beam voltage is above this MEEHV, electron transmission becomes significant and $\alpha(E)$ falls off more steeply than $1/E$, so that $\mathrm{d}E_{abs} / \mathrm{d}E < 0$ for $E >$ MEEHV.

The thickness dependence of the MEEHV is plotted in Fig. 2d. Because thicker films can absorb more electrons at the same incident e-beam energy E, this shifts the MEEHV to larger values for thicker films. The corresponding values of α evaluated at E = MEEHV are shown on the right axis of Fig. 2d. These calculation results show that α value at the MEEHV is almost independent of film thickness, even though MEEHV itself is a strong function of thickness. Of course, these quantities also depend on the material, which underlies the shaded uncertainty bands seen in Fig. 2d which corresponds to the compositional range $\mathrm{SiN}_{1.1}$ - $\mathrm{SiN}_{1.5}$.

From the e-beam matter interaction with its bulb-shaped interaction volume, it is well-known that the location of maximum energy absorption occurs at some finite depth below the specimen surface[39], which is notably different from optical absorption which is maximal at the surface and exponentially decaying into the specimen (the Beer-Lambert law). The depth of the maximum absorbed e-beam energy is much smaller than the e-beam penetration depth R, which itself is defined as the depth at which 99% of the incident electrons have slowed down to rest. The e-beam penetration depth has been extensively studied both analytically [40] and empirically [41], and the expression introduced by Kanaya and Okayama is widely used [40]:

$$R = \frac{0.0276 \times m_A \times N_A \times E^{5/3}}{(Z^{8/9}) \times \rho} \ , \tag{2}$$

where R is the penetration depth in m, E is the incident e-beam voltage in eV, m_{A} is the atomic mass in kg, N_{A} is Avogadro's number, ρ is the density in kg/m^3, and Z is the equivalent atomic

DISTRIBUTION A: Distribution approved for public release.

number of the specimen. It is also interesting to consider the possibility of non-equilibrium phenomena, which have been studied previously in the context of "aloof" scattering of an e-beam in close proximity to solid matter [42]. That study showed that nonequilibrium phenomena are most prevalent at timescales (~10^{-18} - 10^{-17} s) and lengthscales (~1 nm) which are far smaller than those of the present study, suggesting that such nonequilibrium phenomena should only become important for much smaller samples with characteristic lengths below ~10 nm.

Equation (2) shows that the penetration depth increases with the e-beam voltage, and thus so does the depth of maximum e-beam energy absorption. When this absorption depth extends beyond the bottom of the thin film, a significant fraction of the incident e-beam power will transmit through the film, and consequently the absorbed energy will decrease. Thus, the energy absorption coefficient α will also decrease even though there is more input energy from the e-beam. These trends are apparent for *E* larger than ~5 kV in Fig. 2 b and c.

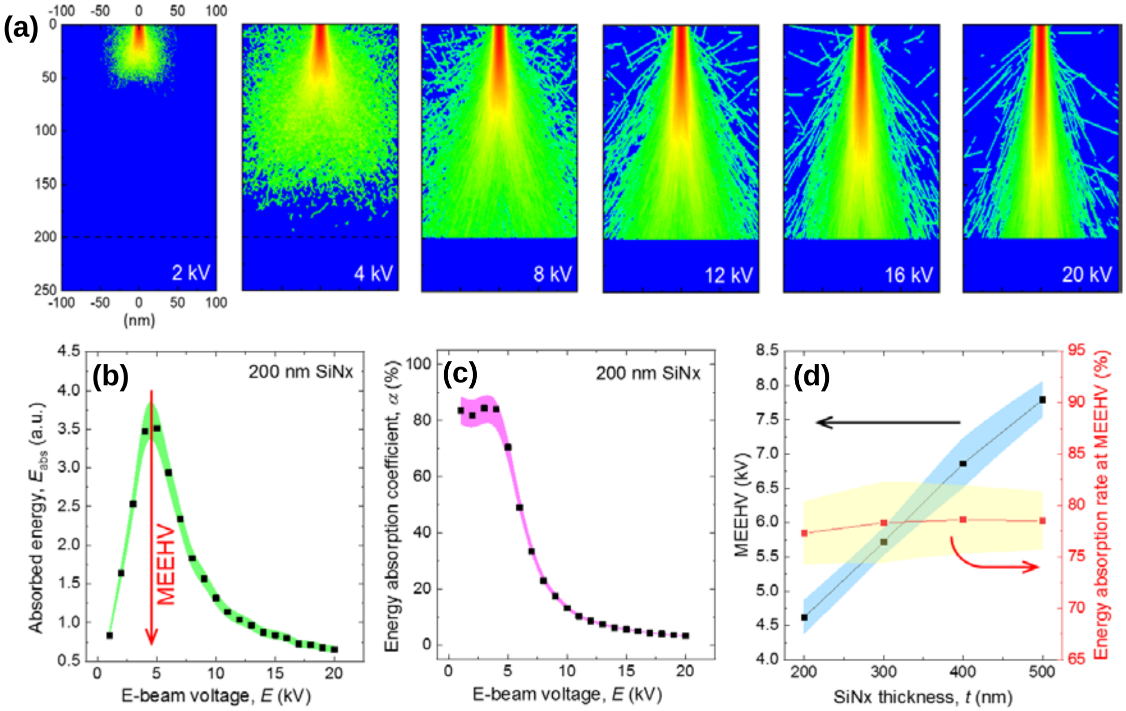

Figure 2. CASINO simulation of electron beam interaction with a 200 nm thick SiNx thin film (x=1.33). (a) The distribution of electron energy deposited in the thin film for different primary e-beam energies. The color scale has arbitrary units proportional to absorbed energy density (J/m3 per incident electron). (b) The total absorbed energy in the thin film for various e-beam voltages.

The MEEHV value is marked. (c) The energy absorption fraction at different e-beam voltages. (d) The MEEHV (left axis) and energy absorption coefficient at that MEEHV (right axis), as functions of film thickness. The shaded bands in b-d represent the effects of varying *x* from 1.1 to 1.5 in the SiN*x* thin film.

b. Experimental energy absorption study of the electron beam in SiN_x thin films

To measure the absorbed e-beam energy in SiN*x* thin films, we microfabricated LPCVD SiN*x* based energy flow calorimeters with built-in platinum resistance thermometers (PRTs) (Fig. 6). The microfabricated low-stress SiN*x* calorimeter devices employed in this work feature a 21 μm (width) × 20 μm (height) suspended island region that is thermally isolated from the substrate by four 300 μm long suspension beams each with a width of 1 μm. The SiN*x* thickness varies from 200 to 500 nm. On top of the SiN*x* thin film is a 4-probe PRT consisting of a long serpentine line (shown in light green in Fig. 6c) with a resistance of ~ 3.7 kΩ between the voltage measuring probes. The serpentine lines are ~250 nm wide and ~ 30 nm thick platinum. As shown in Fig. 6b, one Pt contact pad is integrated into each of the four suspension beams, thereby enabling four-point resistance thermometry of the serpentine PRT.

As shown in Fig. 3, for both the calorimeter and the following 1D ribbon devices, the fabrication process started with low-stress low-pressure chemical vapor deposition (LPCVD) of silicon nitride (SiN*x*) on a 6-inch diameter, 500 μm thick, p-type (100) Si wafer. The nominal thickness of the SiN*x* thin films were confirmed by a profilometer to be within 1% variance, thermal conductivity uncertainty calculations. Then 5 nm of Cr and 30 nm of Pt were deposited by electron beam evaporation. Then a 200 nm SiO_2 hard mask was deposited on the metal by plasma-enhanced chemical vapor deposition (PE-CVD). For patterning, firstly, standard photolithography was performed with an AMSL DUV (deep ultraviolet) stepper Model 5500/300, then the pattern was transferred to the SiO_2 by fluorine-based RIE (reactive ion etch) dry etching. The Cr/Pt was then patterned by ion milling using the hard mask. Secondly, the low-stress nitride was patterned by the stepper and RIE etching. This also defined the etch window for the Si etch. The SiO_2 hard mask was removed by a buffered oxide etch (BOE) solution before releasing the nitride membrane using a 40% KOH solution in DI water.

Note that for the Si etch to release the suspended SiN*x* structures, considering the orientation-selective etch of the Si wafer in KOH solution the etch depth into the wafer (*z*) will be directly

DISTRIBUTION A: Distribution approved for public release.

controlled by the lateral size (*xy*) of the etch window. In the completed device, during the e-beam interaction with the SiN*x* thin film, any transmitted electrons could potentially be reflected by the deep bottom of the Si trench. As depicted in the last panel of Fig. 3, some of these reflected electrons have the potential to return to the suspended SiN*x* structure, which would alter the charge and energy balances as compared to the idealized single-electron-pass configuration of the CASINO simulations. We minimize such potential back reflections by using a large trench depth, which minimizes the "electron view factor" between the bottom of the trench and the suspended SiN*x* beam. Accordingly, the narrower of the two widths of the etch window (*i.e.*, the vertical (*y*) direction in Fig. 3) is defined as 400 μm, which gives the etch depth around 283 μm. We prefer not to etch completely through the wafer in order to maintain the mechanical robustness of the device to increase the yield rate during the subsequent device separation and sample preparation process.

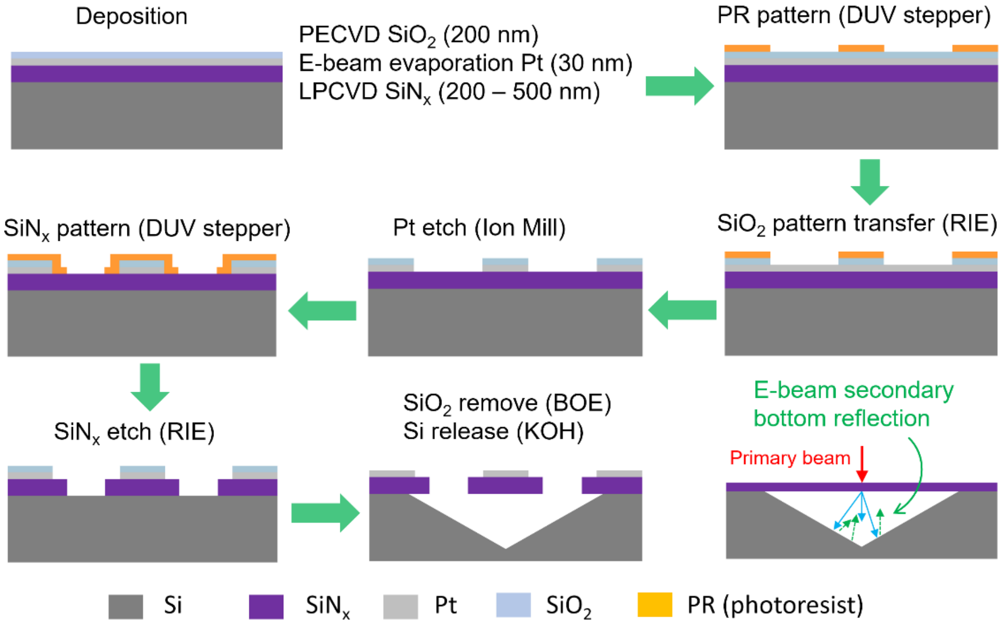

Figure 3. The device fabrication process, starting from layer deposition, then pattern transfer to Pt and SiN*x*, which also defines the Si etch window. The final step is releasing the SiN*x* thin-film structures. The bottom right figure depicts a possible electron beam reflection at the deep bottom of the trench.

The magnitude of the energy flow was quantified by directly measuring the temperature rise of the calorimeter compared to the surrounding temperature T_0, *i.e.*, $\Delta T = T - T_0$. We estimate that there can be an additional temperature rise of up to several degrees Kelvin between the e-beam spot (very center of the island in Fig. 6c) and the average temperature of the island which is determined experimentally from the PRT. This additional superposed temperature rise is unimportant for the calorimetry because it is highly localized primarily to within ~100 nm of the e-beam spot and thus does not reach any of the PRT, as well as the fact that the typical ΔT of the calorimeter is much larger, ~50 K.

We firstly measured the temperature coefficient of resistance (TCR, η) and total thermal conductance (G), it was then mounted in a custom-built SEM holder with electrical feedthroughs for e-beam interaction measurements in a Zeiss Gemini Supra 55VP-SEM. High vacuum conditions (1×10^{-6} torr) make convection losses negligible. Radiation effects are also negligible, as estimated using a conservative (high) estimate of the emissivity of the SiN*x* thin film of about 0.3 (ref. [43]) which corresponds to an estimated error in the ΔT of the PRT island of less than 1%.

To measure small temperature changes with the PRT it is first necessary to calibrate its temperature coefficient of resistance (TCR), denoted with the symbol η, and defined as $\eta(T) = (dR / dT) / R(T)$. Then, the change in the temperature of the resistor (ΔT) can be directly obtained from $\Delta T = \Delta V_s / [I_s \times R_{4p}(T) \times \eta(T)]$, where ΔV_s is the voltage change, I_s is the input sensing current, and R_{4p} is the 4-probe electrical resistance of the PRT serpentine. We measured this ΔR_{4p} using an SR830 lock-in amplifier with a 200–500 nA, 878 Hz sinusoidal excitation current. This sensing current is small enough to cause negligible self-heating (<< 1 mK temperature rise). Calibration details can be found in the next section. Also, to use the calorimeter we need to determine the total thermal conductance (G) of the four suspension beams including the Pt film. Following Ref. [44] this was accomplished in a separate calibration step by passing a DC current through the PRT and measuring the corresponding temperature rise of the central island.

For both calorimeter and 1D ribbon devices, the temperature coefficient of resistance (TCR), η, of the serpentine heater line was determined by measuring the line's electrical resistance $R_{4p}(T)$, at different temperatures T. This calibration was performed separately for every device. For each, the 4-probe resistance was measured by passing a small AC sensing current of amplitude I_{AC} = 300 nA (with frequency f = 878 Hz) through the device, resulting in negligible self-heating. As shown

DISTRIBUTION A: Distribution approved for public release.

in Fig. 4&5, the corresponding AC voltage across the PRT (V_{AC}) was measured with a lock-in amplifier in a 4-probe configuration, and the resistance of the PRT is calculated as $R_{4p}=V_{AC}/I_{AC}$. .

A high-vacuum cryostat was used for all thermal characterization and was evacuated to better than 5×10^{-6} Torr using a turbomolecular pump. A commercial PID temperature controller (Lakeshore 331) was used to stabilize the temperature of the cold head of the cryostat, with a typical stability of ± 0.02 K. Because these experiments make only small excursions from the ambient reference temperature T_0, the resistance can be linearized as

$$R_{4P}(T)=R_{4P}(T_0)\times(1+\eta\Delta T)\,, \tag{3}$$

where $\Delta T=T-T_0$. Therefore

$$\frac{R_{4P}(T)-R_{4P}(T_0)}{R_{4P}(T_0)}=\frac{\Delta R_{4P}(T)}{R_{4P}(T_0)}=\eta\Delta T \tag{4}$$

From the calibration experiments η is determined for every device from its slope of ΔR_{4p} vs. ΔT (*e.g.*, as in Fig. 4d for a representative serpentine). The TCR calibration results for all devices can be found in Table 1.

Table 1. Summary of thermal characterization results of all calorimeter and 1D ribbon devices at room temperature. Error bars correspond to the standard error of the linear regression.

SiN_x Thickness	Calorimeter TCR ($\times10^{-3}$K^{-1})	1D ribbon PRT$_1$ TCR ($\times10^{-3}$K^{-1})	1D ribbon PRT$_2$ TCR ($\times10^{-3}$K^{-1})	Calorimeter beam thermal conductance G ($\times10^{-8}$WK^{-1})
200 nm	1.980 ± 0.012	2.080 ± 0.052	1.987 ± 0.056	3.253 ± 0.006
300 nm	1.590 ± 0.010	2.183 ± 0.051	2.128 ± 0.016	3.453 ± 0.005
400 nm	0.986 ± 0.002	2.906 ± 0.036	2.795 ± 0.020	4.060 ± 0.007
500 nm	0.860 ± 0.003	3.263 ± 0.055	3.252 ± 0.067	3.592 ± 0.008

DISTRIBUTION A: Distribution approved for public release.

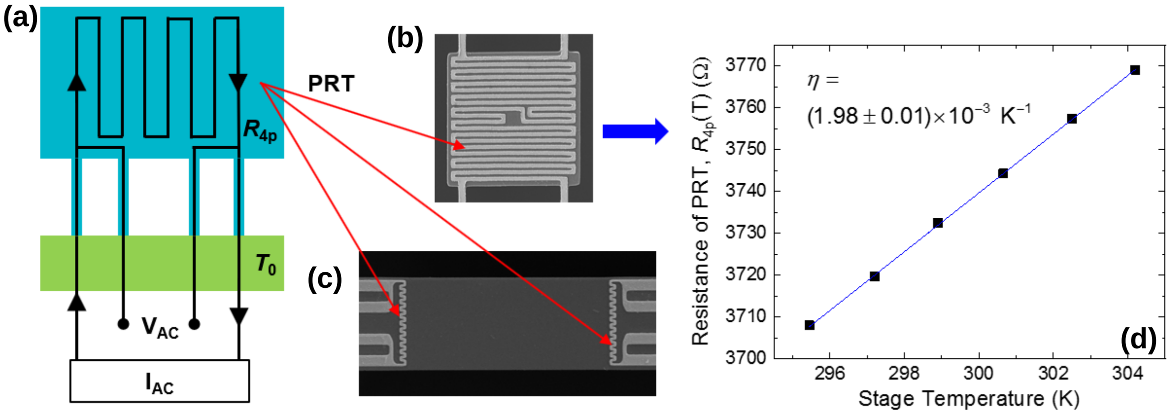

Figure 4. TCR measurement. (a) Schematic of the TCR measurement. (b) Micrograph showing 4-point connections for a PRT on a calorimeter device. (c) Similarly, two PRTs on a 1D ribbon device. (d) Measured resistance of the PRT on the 200 nm thick calorimeter at different cryostat stage temperatures.

Figure 5 shows a schematic of the experimental setup for measuring the total thermal conductance (G) of the suspending beams used in the calorimeter devices. Each device was characterized individually in the same high-vacuum cryostat as used for the TCR measurements described above. A DC current $I_{\rm DC}$ flows through the PRT, generating a Joule heating $Q_h = I_{\rm DC}^2 \times R_{\rm 4p}$ in the island's serpentine line with its resistance $R_{\rm 4p}$. As also indicated in Fig. 4a, a much smaller AC current was superposed on $I_{\rm DC}$ to enable resistance thermometry of $R_{\rm 4p}$ by lock-in detection of $V_{\rm AC}$, which contributes negligible additional Joule heating because $I_{\rm AC} << I_{\rm DC}$. We also considered the finite resistance of each Pt current lead, R_L, which in these devices is typically about half of $R_{\rm 4p}$ and was measured separately by a two-probe method. A combined Joule heat of $2Q_L = 2I_{\rm DC}^2 \times R_{\rm L}$ is dissipated in the two Pt leads that supply the DC current to the central serpentine PRT. The temperature of the heating island remains spatially uniform at T_h, because the internal thermal resistance of the island is much smaller than the combined thermal resistance of the four slender beams, G^{-1} [44]. The Joule heat of Q_L was distributed uniformly along each of the two Pt leads supplying the heating $I_{\rm DC}$ current, yielding a parabolic temperature distribution along these two beams; while a linear temperature profile will occur in the remaining two beams without Joule heating. Following ref. [[44]], the heat conduction to the environment from both Joule-heated beams can be derived as Q_1,

$$Q_1 = 2\times(\frac{G}{4}\times\Delta T_{\mathrm{h}} + \frac{Q_L}{2}) \ , \tag{5}$$

where $G/4$ is the thermal conductance of a single beam, while that from the remaining two beams is

$$Q_2 = 2\times\frac{G}{4}\times\Delta T_{\mathrm{h}} \ . \tag{6}$$

Considering energy conservation for the thin film as $Q_1 + Q_2 = Q_h + 2Q_L$, we then can obtain

$$G = \frac{Q_h + Q_L}{\Delta T_h} = \frac{I_{DC}^2(R_h + R_L)}{\Delta T_h} \ . \tag{7}$$

Q_h and Q_L can be calculated readily from the measured DC current and the voltage drops across the PRT and the PRT leads. ΔT_h is evaluated from the AC measurements of the resistance of the PRT and knowledge of its TCR. As shown in Fig. 5b, G at 300 K is about 3.25×10^{-8} $\mathrm{WK^{-1}}$, in good agreement with the value of 2.73×10^{-8} $\mathrm{WK^{-1}}$ that is calculated from the geometry of the four beams as well as the room temperature thermal conductivity values of SiN*x* and Pt films, i.e., $k_{\mathrm{SiN}x}$=3.61 $\mathrm{Wm^{-1}K^{-1}}$ from this Joule heating measurement, and k_{Pt} = 46.3 $\mathrm{Wm^{-1}K^{-1}}$ is estimated by Wiedemann–Franz law. The measured G values for all calorimeters are summarized in Table 1.

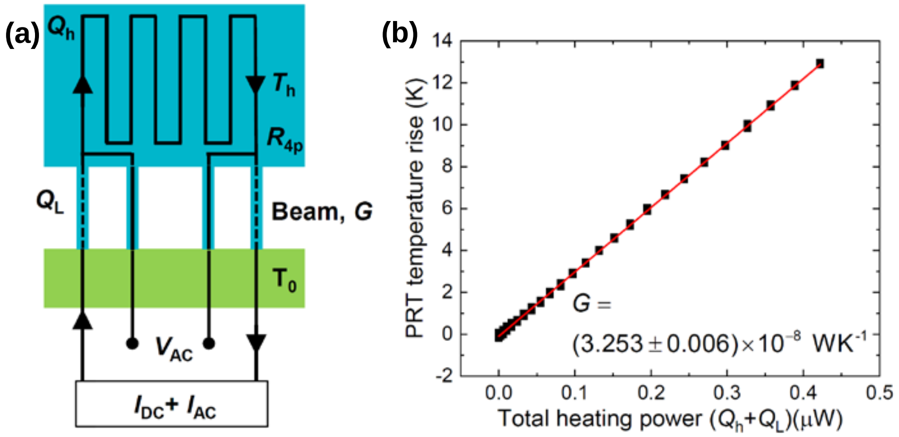

Figure 5. Calorimeter beam thermal conductance measurement details. (a) Measurement schematic. (b) The beam thermal conductance G fitting result for the 200 nm thick device around room temperature. G means the total thermal conductance of the four beams in parallel.

DISTRIBUTION A: Distribution approved for public release.

When the e-beam is focused on the central open square area, approximately 1 μm × 1 μm as seen in the center of Fig. 6c, the absorbed e-beam power will induce a temperature rise ΔT which increases $R_{4\mathrm{p}}$ of the PRT.

This SEM has a field emission electron gun with a sub-1 nm focus beam diameter at >15 kV and ~ 4 nm at 0.1 kV. For e-beam power measurements we use 10,000 times magnification and a 5.5 mm working distance, and position the focused e-beam at the central SiN*x* interaction area indicated in Fig. 6c. Note that the precise location of the e-beam focus position was varied randomly within this ~ $(1\ \mu\mathrm{m})^2$ interaction area from trial to trial to average the absorbed energy analysis. The e-beam current I_{beam} depends on the beam voltage as well as the aperture size in the SEM column, with larger apertures giving higher current [47]. We studied three different current modes by changing the aperture size (30 μm and 20 μm) and/or engaging the high-current mode setting of the SEM. The corresponding beam currents are measured separately using a Faraday cup, with results given in Fig. 7a. A fixed working distance was used because we found that the beam current was slightly changing at different working distances.

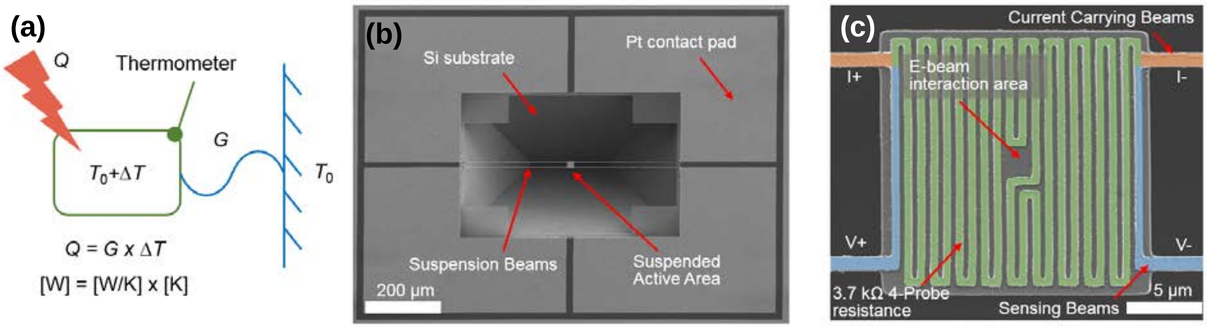

Figure 6. Schematic of the e-beam calorimeter and SEM images of the fabricated devices. (a) The working principle of the calorimeter. The power *Q* can be determined by measuring the temperature change (ΔT) of the calorimeter using the built-in thermometer and known thermal conductance *G*. (b) Low–magnification SEM image of the micro-fabricated SiNx thin-film based calorimeter. The central suspended area of the device is supported by four 1 μm wide, 300 μm long beams, with SiNx thickness varying from 200 to 500 nm among the various devices. (c) False-

color high-magnification image of the central suspended region. The 4-probe platinum resistance thermometer (PRT) is integrated into this island area, with the serpentine line (light green) having a resistance of ~ 3.7 kΩ between the voltage probes (light blue).

c. Comparing the absorbed energy determined from experiment and CASINO

From the calorimeter equation $Q = G\Delta T$ and with ΔT from ΔV_s using Eq. (3), we measured the absorbed heating power for a given calorimeter device as

$$Q = G \times \frac{\Delta V}{I_\mathrm{s} \times R_\mathrm{4p}(T) \times \eta(T)} . \tag{8}$$

For each SiNx device with known thickness, we measured Q as a function of e-beam voltage and find the MEEHV. In fact, for each thickness we actually determine three MEEHV values by using three different beam current modes. To avoid artifacts from the non-constant beam current in actual operation (Fig. 7a), when determining the experimental MEEHV we use the current-normalized absorbed energy which is rescaled by the reference current at 2 kV,

$$\hat{Q}(E) = Q(E) \big/ [I_\mathrm{beam}(E) / I_\mathrm{beam}(2\mathrm{kV})] , \tag{9}$$

where $I_\mathrm{beam}(E)$ is taken from the calibration of Fig. 7a. This normalization is justified because one expects $Q(E) \propto I_\mathrm{beam}(E)$, since each incident electron is an independent event and this was also confirmed by additional experiments. The choice to normalize at the I_beam from 2 kV is arbitrary, and any reference I_beam could be used without affecting the calculated MEEHV values.

The MEEHV(t) results are shown in Fig. 7b, with the blue circles representing the experimental values averaged over the three beam currents, which agree closely with the CASINO results. The relative differences between experiments and simulation are also given in the figure, *e.g.* 6.7 % for t = 200 nm, 3.2% for 300 nm, *etc*. This agreement not only validates the CASINO model discussed in the first section, but also boosts the trust in CASINO to conduct further thermal studies involving electron-matter interaction in SEM. As mentioned in Introduction, previous studies of the e-beam heating of films have been limited to modeling [23, 25, 26], and experiments are lacking. Additionally, we extend the CASINO calculation of MEEHV for thicknesses from 100 to 700 nm, and the full

DISTRIBUTION A: Distribution approved for public release.

range of simulated MHEEV vs. thickness is well-fit with a power law as shown by the red line in the figure.

Knowing this MHEEV(t) relationship has several potential uses. Firstly, in future applications, it could be useful for estimating the thickness of suspended thin films. In this work, we have found the MEEHV by using a PRT to measure the temperature rise, which requires additional microfabrication and instrumentation, but in principle, the temperature rise could instead be measured directly by SEM thermometry which is less accurate but simpler and noninvasive [48]. Note also that knowledge of G is not needed because it never enters into the calculation of the MEEHV (recall that the MEEHV was found in Fig. 7b using arbitrary units on the E axis). Knowledge of the MEEHV is also helpful for thermal metrologies which use the e-beam as a heater, because operating at the MEEHV gives the peak heating which maximizes the signal-to-noise ratio [1-3, 30]. Finally, knowledge of the energy-dependence seen in Fig. 7b is also helpful for optimizing e-beam conditions in standard SEM/TEM imaging of suspended samples. Normally low-E imaging can result in notable charging effects because low-energy electrons will be easily left on the surface, so it is intuitive to increase the beam voltage to reduce the charging effect, but this increased electron beam voltage raises obvious concerns about damaging the sample through overheating. However, Fig. 7b shows that choosing E >> MEEHV may be most favorable of all, because it reduces charging as well as reducing the heat deposited in the sample.

When evaluating the e-beam energy absorption coefficients, α_{CASINO} is statistically determined by tracing all the simulated primary electrons. The experimental values from the calorimeter were calculated as $\alpha = Q/(I_{\text{beam}}E)$ and compared with the CASINO results in Fig. 7c. We determined $\alpha(E, t)$ from the calorimeter for the three different current modes, and in all cases the results are in good agreement with the CASINO simulations as shown in Fig. 7c. This detailed experimental and theoretical understanding of $\alpha(E, t)$ provides the foundation to apply the e-beam as a quantitative heating source for nanoscale thermal metrologies, as demonstrated in the next section for SiNx thin films.

To simplify the energy absorption coefficient of SiNx thin films at different e-beam voltage, for each film thickness in Fig. 7c we empirically fit the e-beam absorption results with a logistic function,

DISTRIBUTION A: Distribution approved for public release.

$$\alpha(E) = A_1 + \frac{A_2 - A_1}{1+(E/E_m)^{\sigma}} \ , \tag{10}$$

where A_2 is the low-E plateau absorptivity, E_m is a characteristic mid-point energy at which $\alpha(E) = (A_1 + A_2)/2$, and σ parameterizes the sharpness of the transition. The fit values of E_m are given in the figure and closely follow a power law $E_\mathrm{m} = at^b$, where the thickness t is in nm and E_m is in kV. This power-law exponent is similar to the value 5/3 in the Kanaya-Okayama range of Eq. (2), and we also find that $E_m(t) = (0.79 \pm 0.01) \cdot \mathrm{MEEHV}(t)$ at least over this range of thicknesses. Such similarity is not surprising considering that they all originate from the same physical mechanism of the e-beam penetration depth reaching and then exceeding the film thickness.

For each plot in Fig. 7c, there is relatively large data variation for $E < E_\mathrm{m}$ and better consistency for $E > E_\mathrm{m}$. The absorption coefficient α shown here is an average over various e-beam spot locations in the central ~1 μm interaction area in Fig. 6c. For lower e-beam voltages, we found that the charging effects varied significantly among these spot locations, causing the notable variation. This effect was more limited when higher e-beam voltage ($E > E_\mathrm{m}$) was applied.

Finally, in Fig. 7d we collapse all of the results from Fig. 7c into a single universal logistic function, $\alpha(E,t) = A_1 + \frac{(A_2 - A_1)}{1+[(E/E_\mathrm{m}(t)]^{\sigma}}$, where $E_m(t) = cat^b$ and the fit values for a, b, c, A_1, A_2, and σ are given in the figure for SiN*x* and are independent of E and t. The points shown in this plot comprise all 16 sets of data from Fig. 7c, both experimental and from CASINO, with the *x*-axis re-scaled by dividing E by each thickness' corresponding $E_\mathrm{m}(t)$. The generally excellent collapse of data seen in Fig. 7d after this re-scaling confirms that for each thickness there is fundamentally only one characteristic energy scale, whether it is discussed as MEEHV(t), $E_\mathrm{m}(t)$, or the inversion of Eq. (2) after equating R and t, namely, $E_\mathrm{KO}(t) = (\frac{\rho z^{\frac{8}{9}} t}{0.0276 m_\mathrm{A} N_\mathrm{A}})^{\frac{3}{5}}$.

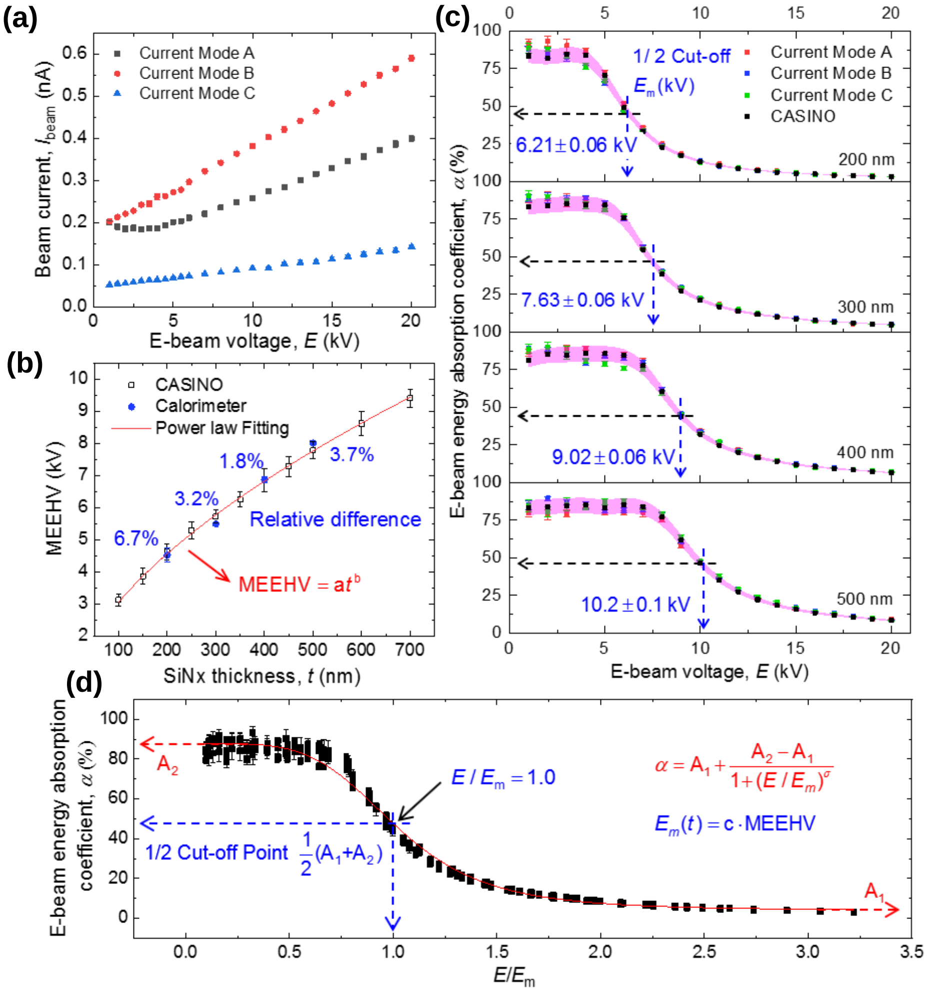

Figure 7. The thickness and current dependence of e-beam absorption. (a) Three current modes used in this work, measured using a Faraday cup. Mode A corresponds to 30 μm aperture size in the normal current setting, with a typical error bar 1.1% - 3.8%. B corresponds to 30 μm aperture size in the high current setting, with a typical error bar 1.0% - 3.4%. C corresponds to 20 μm aperture size in the normal current setting, with typical error bar 1.7% - 4.7%. (b) Comparison of MEEHV values determined theoretically from CASINO and experimentally from calorimeter devices (average of three current modes, with error bars showing their standard deviation). The listed percentages give the relative difference between theory and experiment. The power-law fit to the CASINO results yields $a = 0.22 \pm 0.02$ kV and $b = 0.57 \pm 0.02$, with t in nm. (c) The e-beam energy absorption coefficients from CASINO (pink shaded band represents the effect of varying x from 1.1 to 1.5) compared with experimental results from SiNx based calorimeter devices of four thickness each with three current modes. The CASINO results for 200 nm thick SiNx are repeated

from Fig. 2c. A logistic function is used to fit the results for each thickness, with the listed midpoint cut-off energies, E_m. (d) Plot of all 16 sets of data from (c) after rescaling E/E_m (points), and a fit with a universal logistic function (line). $A_1 = 4.07 \pm 0.15$, $A_2 = 88.9 \pm 0.4$, and $c = 0.76 \pm 0.01$.

d. Demonstration of e-beam as a quantitative heating source for thermal metrology: measuring the thermal conductivity of SiN*x* thin films

Building on the above calorimeter and CASINO study of the e-beam energy absorption in SiN*x* thin films, we are now able to use the e-beam for quantitative thermal analysis. In this section, we will demonstrate using the e-beam heater to determine the in-plane thermal conductivity of LPCVD SiN*x* thin films, and the results are confirmed by independent measurements using a Joule-heating method. As mentioned above, amorphous silicon nitride is commonly used in many microelectronic and MEMS devices, including suspended structures [36, 37, 49]. As such, knowledge of the in-plane thermal conductivity of SiN*x* films is important as micro-fabricated heaters and thermal sensors are thermally isolated from the environment using these suspended structures. Furthermore, the thermal conductivity of SiN*x* films can depend on stoichiometry, growth conditions, and film thickness, so it is generally not accurate to simply take a reference value from the literature.

As shown in Fig. 8a, we prepared free-standing SiN*x* ribbon devices using the same processing steps as the calorimeter. The suspended area is 430 µm long and 12 µm wide which justifies approximating the heat flows as 1D along the *x*-direction of the SiN*x* ribbon. The SiN*x* ribbon thickness of different devices ranges from 200 to 500 nm, and as shown in Fig. 8d. Measurements of the MEEHV vs. thickness for these suspended ribbon devices shows nearly identical response as the previous measurements on calorimeter devices and CASINO simulations. At the central area of the ribbon (Fig. 8b) there are two 4-probe PRTs which can serve as both heater and thermometer, separated by a distance L=30 µm. Each PRT's 4-probe electrical resistance is around 550 **Ω**, and their TCRs are calibrated to measure the local temperature rise.

The basic principle of the thermal conductivity measurement is depicted in Fig. 8b&c. The e-beam was used as a line heat source at a location x, causing steady-state 1D heat flow (along ± x directions) in the SiN*x* ribbon to the Si substrate which acts as a heat sink at T_0. Two PRTs measured the resulting temperatures T_1 and T_2 as functions of the e-beam location x, which as detailed next can be used to determine k, the in-plane thermal conductivity of the SiN*x* thin film.

In developing the detailed thermal analysis model, convection and radiation losses were both estimated to be negligible. To experimentally justify a 1D analysis along the *x*-direction, we first used local e-beam heating to investigate possible 2D effects. With the e-beam in spot mode at a fixed *x* coordinate near $x = 0$, we moved the e-beam along *y*, and found that the temperature rises at each of the two PRTs were independent of the e-beam spot's *y* location to within 2%. This variation is mainly random but higher whenever the e-beam focused on some rough areas (appearing as whiter dots in the SEM image) which affects the interaction between e-beam and the thin film. To average out these variations and even better approximate 1D heat conduction, for all subsequent measurements we control the e-beam to approximate a line heating source, by rapidly scanning the focused e-beam along the *y*-direction between +5 µm and −5 µm. This scanning is realized by a Python-based software platform (ScopeFoundry)[50] instead of using the default Smart SEM software from Zeiss. The scanning rate is set as 500 kHz.

In the thermal model, define R_L as the thermal resistance (K/W) of each of the ~200 μm long suspended ribbon sections between the heat sink and the PRTs. Due to the symmetry of the microfabrication, the two R_Ls are nominally identical, namely the left R_L between T_0 and T_1, and the right R_L between T_0 and T_2. Note that R_L includes the parallel conduction pathways of the SiN*x* thin film and the Pt lines on top. Similarly, the thermal resistance of the SiN*x* between the two PRTs is

$$R_S = \frac{L}{A \times k}, \tag{11}$$

where $A = wt$ is the cross-sectional area of the ribbon, w = 12 µm is the ribbon width, L = 30 µm is the distance between two PRTs, and *k* is the in-plane thermal conductivity of the SiN*x* thin film.

With the e-beam heating line localized a station *x* as indicated in Fig. 8b, two equivalent expressions for the heat flow to the left are

$$Q_1 = \frac{\Delta T_1}{R_L} = \frac{\Delta T_i(x) - \Delta T_1(x)}{R_i(x)} \ , \tag{12}$$

where $\Delta T_1 = T_1 - T_0$ is temperature rise measured by left PRT, $\Delta T_i(x) = T_i(x) - T_0$ represents the temperature rise at the e-beam heating position *x* which cannot be directly measured in this

DISTRIBUTION A: Distribution approved for public release.

experiment, and $R_i(x)=(L/2+x)/(kA)$ is the thermal resistance between the e-beam heating position x and the left PRT. Likewise, considering the heat flow going to the right, we have

$$Q_2=\frac{\Delta T_2}{R_L}=\frac{\Delta T_i(x)-\Delta T_2(x)}{R_s-R_i(x)}. \tag{13}$$

From the overall energy balance, the total absorbed e-beam energy (Q) is finally conducted to the heat sink through both ends ($Q = Q_1+Q_2$), so we have

$$Q=\frac{\Delta T_1+\Delta T_2}{R_L}. \tag{14}$$

Then we eliminate ΔT_i from Eqs (12) and (13) to have $\Delta T_1 R_i-\Delta T_2(R_S-R_i)=(\Delta T_2-\Delta T_1)R_L$. Differentiating this equation with respect to x and using Eq (14) to represent R_L, we can express the thermal conductivity k as

$$k=Q\times\frac{(\Delta T_1+\Delta T_2)-\frac{\partial\Delta T_2}{\partial x}\times L}{(\Delta T_1+\Delta T_2)\times A\times\frac{\partial(\Delta T_2-\Delta T_1)}{\partial x}}, \tag{15}$$

where Eq. (14) also shows that the sum $(\Delta T_1+\Delta T_2)$ is independent of x, which further implies $\partial\Delta T_1/\partial x=-\partial\Delta T_2/\partial x$. In the experiment, we determine $\partial\Delta T_1/\partial x$ and $\partial\Delta T_2/\partial x$ by placing the e-beam heating line at different x positions. Here, we use Current Mode A and operate at each thickness' corresponding MEEHV value to maximize the signal-to-noise ratio. Typical results for the 200 nm thick ribbon device are shown in Fig. 8e, which confirms the expected symmetries of $\partial\Delta T_1/\partial x=-\partial\Delta T_2/\partial x$ to within 1.5%. For this device, k is found from Eq. (15) to be 3.84 ± 0.24 $\mathrm{Wm^{-1}K^{-1}}$.

The results for thickness-dependent thermal conductivity using this new e-beam based method are plotted as empty squares in Fig. 10b, which shows that k increases from 3.84 to 5.23 $\mathrm{Wm^{-1}K^{-1}}$ as t increases from 200 to 500 nm. We have shown error bars of with 7%, the largest sources of error include fitting results of $\partial\Delta T_1/\partial x$ and $\partial\Delta T_2/\partial x$, and the absorbed e-beam energy evaluation from the calorimeter. The general trend of increasing $k(t)$ is very well established for thin films due to boundary scattering of long mean-free-path phonons at the film surfaces which reduces k for small

DISTRIBUTION A: Distribution approved for public release.

t, as is frequently modeled using the Fuchs-Sondheimer solution of the Boltzmann transport equation[51-53]. For the amorphous silicon nitride studied in this work, its thermal conductivity has been previously reported to contain a significant contribution from long-mean-free-path propagons as compared to nonpropagating modes,[54] so thin-film size effects play a role in thermal conduction. Figure 10b also shows that these measured *k* values are comparable to other literature reports for suspended LPCVD SiN*x* with a thickness below 800 nm. 50 and 200 nm thick suspended LPCVD SiN*x* membranes were ~2.5 and ~4.5 $Wm^{-1}K^{-1}$ respectively [5]. ~2.8 $Wm^{-1}K^{-1}$ was reported for a 100 nm thick LPCVD SiN*x* film [55], ~3.3 $Wm^{-1}K^{-1}$ for 500 nm thick SiN*x* bridge [6], *etc*.

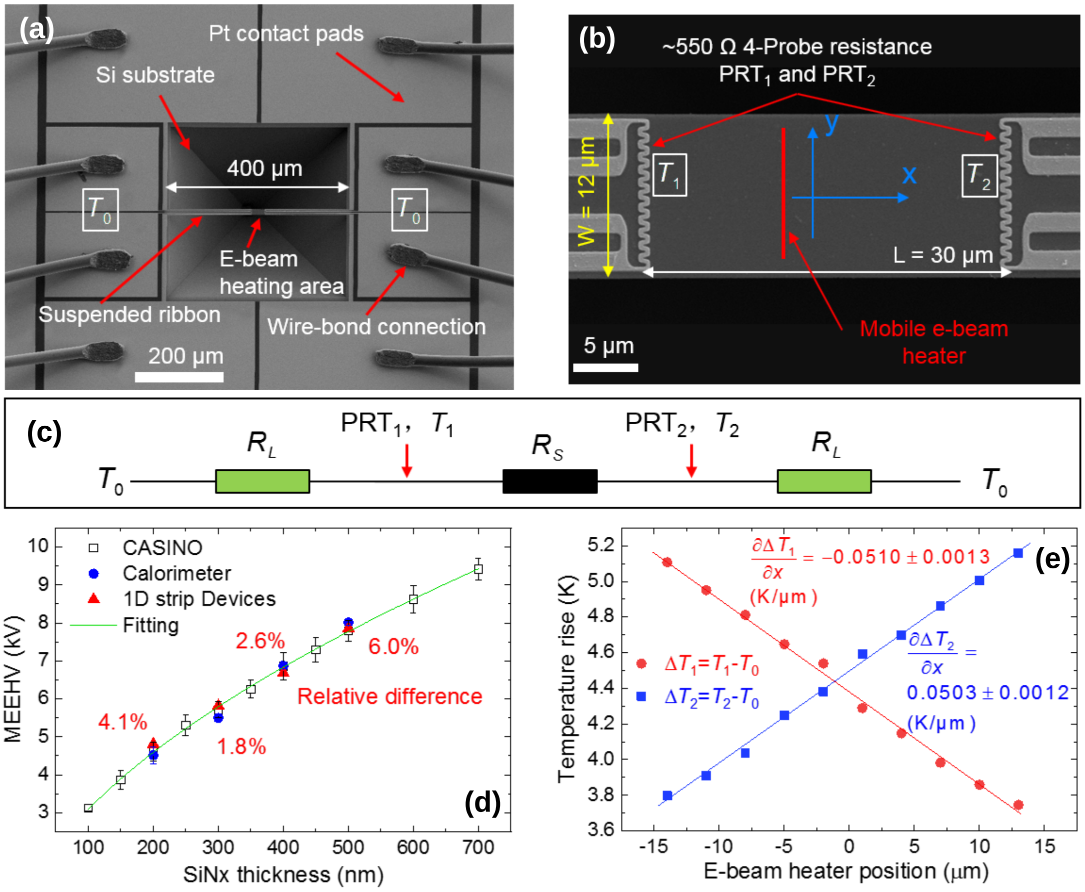

Figure 8. 1D ribbon device structure for SiN*x* thermal conductivity measurement using e-beam heating. (a) Low magnification SEM image of the microfabricated device. The suspended portion is 430 μm long (considering undercut) and 12 μm wide, with SiN*x* thickness ranging from 200 nm to 500 nm. (b) High magnification image of the central suspended region which is also the e-beam heating area. (c) The thermal circuit of the 1D SiN*x* ribbon device. R_S represents the thermal

resistance between the two PRTs. (d) The thickness of these device is confirmed by their MEEHVs (red triangles), which lies very close to previous results repeated from Fig. 7b. (e) Temperature rise at the two PRTs as a function of e-beam heater location *x*, for the 200 nm thick device.

To validate the *k*(*t*) measurements from the e-beam heating method, we also implemented a Joule heating method to independently measure *k* in the same structures. In this technique, we used PRT_1 as a heater and both PRTs as temperature sensors. The analysis would be simplest if the Joule heating were localized purely at PRT_1, but the two DC current-carrying leads also contribute Joule heat which must be taken into account. Therefore we conducted two sets of experiments and used a superposition argument to determine the equivalent response to localized Joule heating at only the left PRT (Q_{PRT1}), called Case C.

For the Joule heating method depicted in Fig. 8 we apply a DC current to generate localized Joule heating at PRT_1, similar to a localized e-beam line heater. However, as shown in Fig. 9a, this causes additional Joule heating in the two current leads, which we take into account using measurements with two different connections. In case A of Fig. 9a, the current is applied between contact pad 1 and contact pad 4, while in case B, the current was applied between contact pads 1 and 2, thereby bypassing the PRT. These measurements are analyzed using a superposition argument to deduce the corresponding Case C, as discussed next.

(a) Superposition argument

From the principle of linear superposition, we recognize that Case A is very nearly equivalent to Case B plus Case C, where Case C corresponds to a localized line heat source only at the PRT which would be easiest to analyze. This superposition argument is not exact because in case A leads 1 and 4 experience Joule heating, while in Case B it is leads 1 and 2. However, because the heat transfer is predominantly along the *x*-direction, and leads 2 and 4 differ only in their y coordinate, this distinction will have very little impact on the heat conduction problem. Another imperfection in the superposition is the Joule heating in Case B in the small metal connection between leads 1 and 2 (purple area in Fig. 9b, 2 μm × 0.75 μm), which is not present in Case A. Overall, the equivalence C ≈ A − B holds true to a very good approximation, as confirmed by 3D numerical simulations. Therefore, for the analysis of the Joule heating approach for extracting *k* of the SiN*x* film, we measure T_1 and T_2 as functions of I_{DC} for Cases A and B, and then determine the equivalent T_{1C} and T_{2C} by subtraction, for example $T_{1C}(I_{DC}) = T_{1A}(I_{DC}) - T_{1B}(I_{DC})$. Note that for the purposes of Fig. 9(a), I_{DC} has been expressed as a corresponding Q_{PRT1}, this is defined as $I_{DC}^2 R_{4p}$, even for Case B with no heat actually dissipated in PRT_1. This transformation to Case C simplifies the heat conduction analysis leading to Eqs. (11) - (15). Also, considering the obvious left-right symmetry of the 1D ribbon design, we repeat these k measurements using mirrored connections, i.e. Joule heating PRT_2 rather than PRT_1. For a given device, the measured k values are expected to be the same for measurements using PRT_1 and PRT_2, and the results in Table 2 confirm that they differ by no more than ±4%.

(b) Metal line leads resistance effect

We analyze the differences between these two cases by considering the various metal line segments making up the leads, depicted in Fig. 9b.

For a single platinum line segment of length L, by Pouillet's law, its electrical resistance is $R = \rho \times L/A$, where ρ is the electrical resistivity and $A=Wt$ is the cross-sectional area, where W is the linewidth and t=30 nm is the thickness. For convenience introduce $\varphi = (\rho / 3\mathrm{t})$ which is simply 1/3 times the sheet resistance, thus $R = (3L/W)\varphi$. This factor of 3 is chosen to yield convenient integer values later. Thus, for example, the green section in Fig. 9b has L/W = 20 and so $R = 60\varphi$. Similar calculations give the other φ values listed in Fig. 9b.

Using $R_{i\text{-}j}$ to denote the two-probe electrical resistance between pads i and j, from Fig. 6c and using the φ values enumerated in Fig. 9b we find $R_{1\text{-}4}=920\varphi+R_{4p}$. Similarly, from Fig. 9d we have $R_{1\text{-}2}=889\varphi$. Here, we can directly measure R_{4p} by a four probe configuration, and $R_{1\text{-}2}$ and $R_{1\text{-}4}$ by a two probe configuration. However, the Pt sections indicated in green and yellow in Fig. 9b are substrate-supported with excellent heat sinking, and therefore do not contribute to the actual Joule heating. Therefore define R_B as the unsupported portion of $R_{1\text{-}2}$, and thus $R_B=809\varphi$. These geometric calculations allow us to eliminate φ to evaluate R_B directly from the measured $R_{1\text{-}2}$, using $R_B=(809/889)R_{1\text{-}2}$. Similarly, define R_A as the unsupported portion of $R_{1\text{-}4}$, and thus $R_A=800\varphi + R_{4p}$, whereas $R_{1\text{-}4}=920\varphi+R_{4p}$; so eliminating φ gives $R_A=(20/23)(R_{1\text{-}4}-R_{4P})$. Using the real electrical resistance for both case A and case B, we can evaluate the Joule heating energy correspondingly. By subtracting the temperature rise of two PRTs and the Joule heating energy of case B from case

DISTRIBUTION A: Distribution approved for public release.

A, we can have the case C which can be directly used to determine the thermal conductivity of SiN*x* thin film.

(c) Thermal conductivity of SiN*x* ribbon from Joule heating method

In Joule heating method, we can eliminate R_L from Eqs 11 and 13 to have

$$\frac{Q_{\mathrm{PRT1\_1}}}{Q_{\mathrm{PRT1\_2}}} = \frac{\Delta T_{1\mathrm{C}}}{\Delta T_{2\mathrm{C}}}. \tag{16}$$

From Eqs 12 and 14, we eliminate R_L to express R_S as

$$R_{\mathrm{S}} = \frac{(\Delta T_{1\mathrm{C}} - \Delta T_{2\mathrm{C}}) \times (\Delta T_{1\mathrm{C}} + \Delta T_{2\mathrm{C}})}{Q_{\mathrm{PRT1}} \times \Delta T_{2\mathrm{C}}}. \tag{17}$$

Differentiating Eq 16 and Eq 17 with respect to Q_{PRT1}, we can rewrite Eq 17 as

$$R_{\mathrm{S}} = \left(\frac{\partial T_{1\mathrm{C}} / \partial Q_{\mathrm{PRT1}}}{\partial T_{2\mathrm{C}} / \partial Q_{\mathrm{PRT1}}} + 1\right) \times \left(\frac{\partial T_{1\mathrm{C}}}{\partial Q_{\mathrm{PRT1}}} - \frac{\partial T_{2\mathrm{C}}}{\partial Q_{\mathrm{PRT1}}}\right). \tag{18}$$

Rearranging Eq 18 gives the *k* expression as Eq 15.

Table 2. Complete in-plane thermal conductivity measurement results from e-beam and Joule heating methods. The 1st Joule heating method is by using $\mathrm{PRT_1}$, and 2nd is by using $\mathrm{PRT_2}$.

Device Thickness (nm)	E-beam heating method ($\mathrm{Wm^{-1}K^{-1}}$)	1st Joule heating method ($\mathrm{Wm^{-1}K^{-1}}$)	2nd Joule heating method ($\mathrm{Wm^{-1}K^{-1}}$)	Joule heating method average value ($\mathrm{Wm^{-1}K^{-1}}$)
200	3.84 ± 0.24	3.54 ± 0.13	3.68 ± 0.12	3.61 ± 0.18
300	4.09 ± 0.20	3.91 ± 0.16	3.95 ± 0.15	3.93 ± 0.22
400	4.48 ± 0.22	4.34 ± 0.13	4.21 ± 0.12	4.28 ± 0.18
500	5.23 ± 0.14	4.95 ± 0.12	5.05 ± 0.12	5.00 ± 0.17

DISTRIBUTION A: Distribution approved for public release.

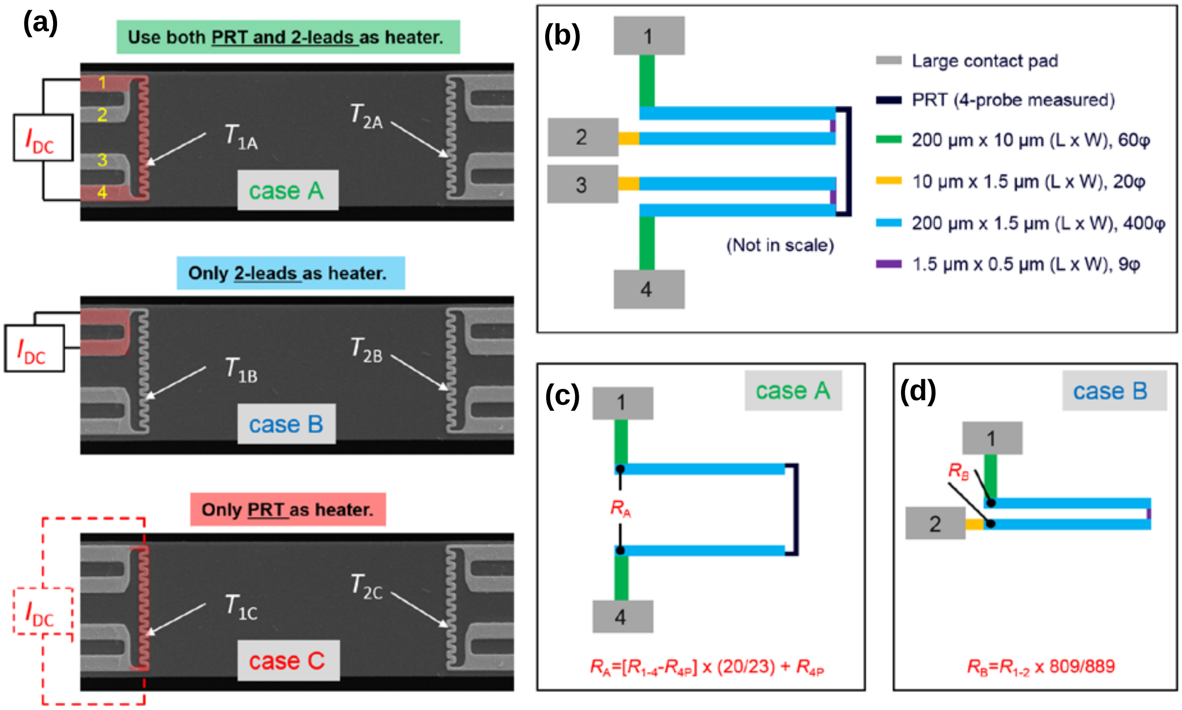

Figure 9. Variable connection scheme to realize the equivalent of localized Joule heating, in which the preferred situation, Case C, is approximated by the subtraction A - B. (a) Experimental connections for Cases A and B, and depiction of the ideal case C. Red shading indicates regions of Joule heating. (b) Schematic of the electrical resistances of the various leads comprising the PRT. (c) Contributions to the resistance of Case A. (d) Contributions to the resistance of Case B.

Focusing on Case C, just as in the e-beam heating method the localized Joule heating from PRT_1 will flow to both to left and right heat sinks. Considering the heat flow to the left ($Q_{\text{PRT1\_1}}$), we have

$$Q_{\text{PRT1\_1}} = \frac{\Delta T_{1\text{C}}}{R_L}, \tag{19}$$

where $\Delta T_{1\text{C}} = T_{1\text{C}} - T_0$ is the temperature rise of heating PRT_1 for case C. Similarly, the heat flow to the right is

$$Q_{\text{PRT1\_2}} = \frac{\Delta T_{1\text{C}} - \Delta T_{2\text{C}}}{R_S}, \tag{20}$$

DISTRIBUTION A: Distribution approved for public release.

also,

$$Q_{\mathrm{PRT1\_2}} = \frac{\Delta T_{\mathrm{2C}}}{R_L}, \tag{21}$$

where ΔT_{2C} is the temperature rise of the sensing PRT_2. Also from the overall energy balance, the Joule heating at the left PRT (Q_{PRT1}) is finally conducted to the heat sink through both ends, $Q_{\mathrm{PRT1}} = Q_{\mathrm{PRT1\_1}} + Q_{\mathrm{PRT1\_2}}$, so we have

$$Q_{\mathrm{PRT1}} = \frac{\Delta T_{\mathrm{1C}} + \Delta T_{\mathrm{2C}}}{R_L}. \tag{22}$$

So the thermal conductivity of the SiNx thin film can be determined by

$$k = \frac{L}{A \times \left(\frac{\partial T_{\mathrm{1C}} / \partial Q_{\mathrm{PRT1}}}{\partial T_{\mathrm{2C}} / \partial Q_{\mathrm{PRT1}}} + 1\right) \times \left(\frac{\partial T_{\mathrm{1C}}}{\partial Q_{\mathrm{PRT1}}} - \frac{\partial T_{\mathrm{2C}}}{\partial Q_{\mathrm{PRT1}}}\right)}. \tag{23}$$

An example of the raw data for this measurement is given in Fig. 10a for a 200 nm thick SiNx thin film. Using Eq. (15) we find $k = 3.61 \pm 0.18\ \mathrm{Wm^{-1}K^{-1}}$ which is only 6.3% smaller than the k value determined from the e-beam heating method. These measurements for all four thicknesses are compared in Fig. 10b, with mutual agreement between e-beam and Joule heating measurements always better than 7%. The error bars for the Joule heating results come from the uncertainty in TCR and electrical resistance and the variation between k values as determined using PRT1 (e.g. as shown in Fig. 10a) and PRT2 (not shown in Fig. 10a).

Comparing heating by the e-beam versus Joule heating of a PRT, the e-beam heating approach offers several advantages. First, although the e-beam based k measurements in this study required additional microfabrication to create the PRT, in principle the temperature could instead be measured directly using the SEM [48, 56] or TEM [57-61] itself. This will greatly simplify the microfabrication and make the e-beam heating and sensing at arbitrary locations and with various shapes. Second, an e-beam line heater can be narrower than a lithographically defined PRT, better concentrating the heat source and simplifying analysis. Similarly, the e-beam better approximates a sheet source in the yz plane, whereas a PRT heater is a surface source whose heat must diffuse further down in z-direction before it can flow purely along $\pm x$. On the other hand, the Joule heating delivered by a PRT can be measured more accurately, and has the potential to deliver much larger

DISTRIBUTION A: Distribution approved for public release.

heating powers and thus greater temperature differences than the e-beam. This last point can be a serious restriction and means the e-beam heating approach is most appropriate for samples of relatively low thermal conductance *G*, i.e. long, thin, and low-*k*.

The thermal conductivity measurement technique demonstrated here on silicon nitride can in principle also be adapted to study thin films of other materials, such as polysilicon, silicon carbide, and metals. Although the results from the first part of this study show that the e-beam energy deposition as calculated by CASINO is reliable for silicon and nitrogen, if extending this new thermal metrology to other materials additional measurements of the energy absorption are recommended before fully relying on such simulations.

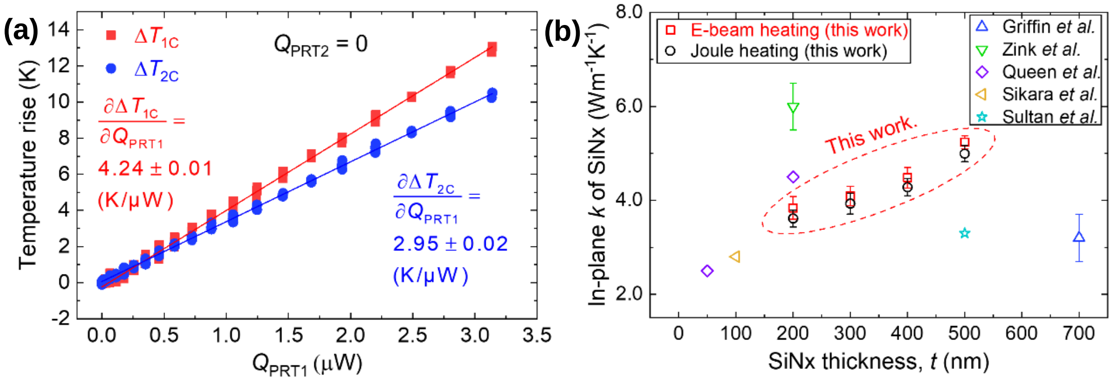

Figure 10. Joule heating approach to measure *k* of the 1D ribbon devices. (a) Results for the 200 nm thick device: temperature rises of the two PRTs in response to Joule heating by PRT1. (b) Comparison of SiN*x* thermal conductivity at room temperature as determined by the e-beam heating and Joule heating methods. Literature results are from Refs. [4-6, 55, 62, 63]

e. Discussion

We demonstrate how an e-beam can be used as a quantitative mobile heating source and apply it to perform thermal measurements at the nanoscale. Experiments using microfabricated calorimeter SiN*x* devices of varying film thickness and e-beam energy validate the electron energy deposition predictions of the widely-used Monte Carlo simulation program CASINO. These energy absorption results provide a foundation to exploit the e-beam as a quantitative mobile heating source for nanoscale thermal metrology. We demonstrate this capability by measuring the in-plane thermal conductivity of SiN*x* thin films of varying thickness, with results in good agreement with independent measurements using a Joule heating method. This study shows how the electron beam

DISTRIBUTION A: Distribution approved for public release.

in an SEM has the potential to develop into a practical tool for non-contact thermal measurements at the nanoscale.

B. Non-diffusive heat transport induced by e-beam heating on SiNx thin film

As we mentioned in the first section (background), we believe that the e-beam can provide the nanoscale heating source for advanced application.

As we know, the heat transport carriers (phonons) in the SiNx thin film can be divided into two groups: a diffusive group with MFPs (mean free paths) shorter than the characteristic distance and a ballistic group with MFPs longer than the characteristic distance. The characteristic distance here is the distance between e-beam heating position and PRT. In this case, when this characteristic distance is comparable with MFPs of the SiN*x* thin film. The effective in-plane thermal conductivity will decrease from an increasingly larger portion of phonons joining the ballistic group as the distance is reduced. With constant energy input (e-beam heating), the thermal energy dissipating to PRT1 will decrease due to increased total thermal resistance. As a result, the temperature rise measured by PRT1 will be smaller than the estimation from classic Fourier's law.

As shown in Figure 11 below, the smallest characteristic distance we have is 1 µm and only 500 nm away from the PRT edge. And the temperature measured by the PRT will average this 1 µm wide area. The experiment was conducted in room temperature. However, as shown in Figure 11 and Figure 12 (for another three SiN*x* sample with different thickness), the temperature rise measured by PRT at this characteristic distance still falls into the linear region, so we did not visualize non-diffusive transport. This means that the characteristic distance is still larger than the MFPs of SiNx. In this work, the SiNx is from chemical vaper deposition and amorphous, and the MFPs are in the order of sub-10 nm.[54] Only the characteristic distance is in the similar order that we can look into the non-diffusive transport and develop a nanoscale MFP spectroscopy technique like this [64] but with less nano-fabrication work. Considering both the material itself (SiN*x* has very short MFP) and the PRT structure (1 µm width), we did not get chance to demonstrate this in this work.

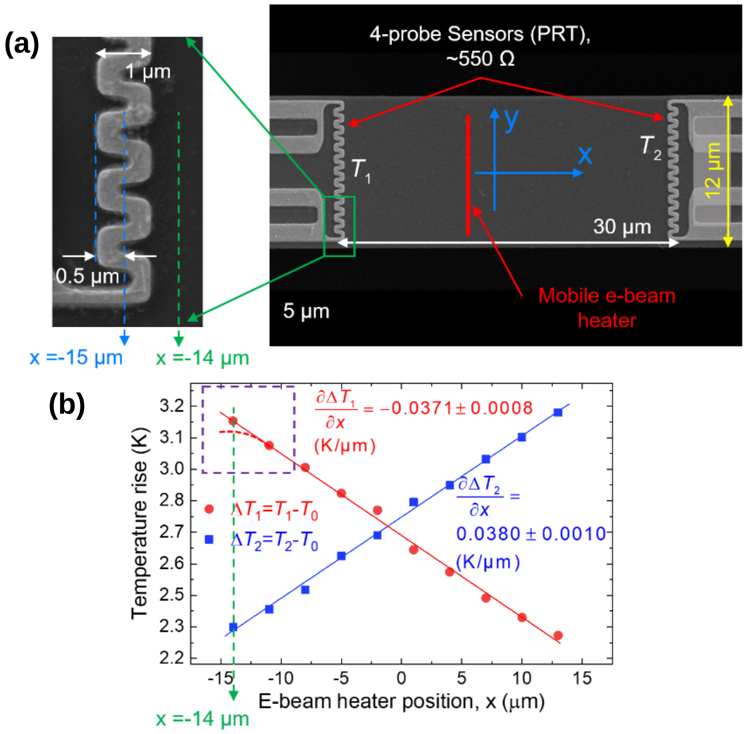

Figure 11. (a) 1D ribbon device structure for SiNx thermal conductivity measurement using e-beam heating with detailed SEM structure, the smallest characteristic distance (the distance between e-beam heating position and PRT) is 1 um. (b) Temperature rise at the two PRTs as a function of e-beam heater location *x*, for the 200 nm thick device, the red dashed line of ΔT_1 is the expected signal if the characteristic distance is in the same order of MFP of SiN*x*.

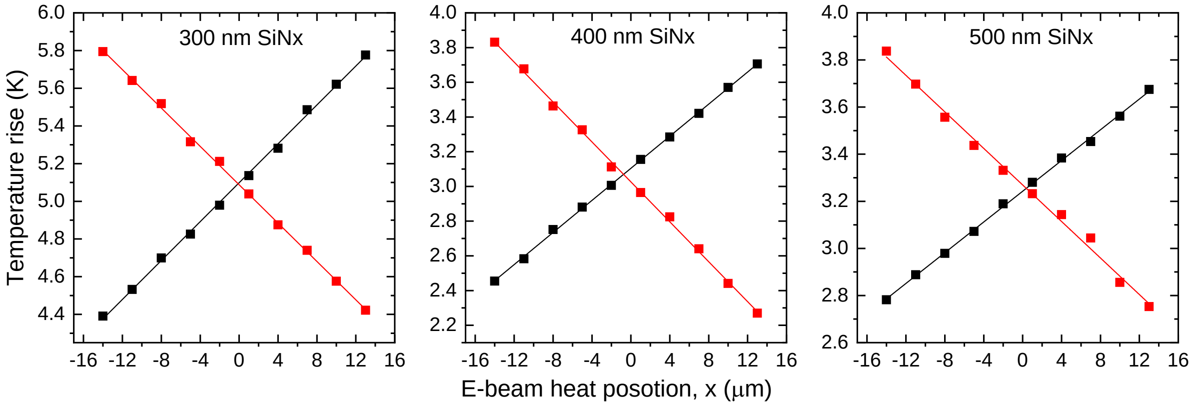

Figure 12. The temperature rise of two PRTs as a function of e-beam heater location *x*, for 300 nm, 400 nm, and 500 nm thick SiN*x* thin film samples.

However, we propose that by using narrow PRT (~100 nm width) on crystal material (such as crystal-Si) will allow us to reconstruct MFP distribution of interested materials. The reconstructed MFP distributions will help device and structure design in optimizing thermal management of nano-electronics. From this point of view, we can conclude that the e-beam heating can provide nanoscale heat source to directly study the non-diffusive heat transport. And the flexibility of moving nanoscale heating source by e-beam will not be easily realized by other technique.

C. Thermal diffusivity determined by modulated e-beam heating

For the 1D strip structure, we can also determine its thermal properties using modulated e-beam heating source. We used a beam blanker to modulate the e-beam from SEM. A function generator is used to output a TTL square wave signal and control the electron-beam blank controller. The e-beam blank controller has a rise time of 50 ns and can be tuned to up to 1MHz. Then, a square-wave like heating source can be generated in SEM.

As shown in Figure 13 (a), the modulated e-beam heating source is focused on the marked red spot location with spot mode. As demonstrate above, the temperature induced by e-beam is almost constant with different scanning modes (spot and raster scan with high frequency). The frequency sweep induced temperature change of PRT1 is represented by the voltage amplitude as shown in Figure 13 (b). We can roughly find the cut-off frequency as around 30 Hz as marked with green cross. However, the 1D strip structure is not strictly uniform due to the PRT metal layer. So a numerical simulation solution to find the thermal properties of SiNx thin film will be more practical.

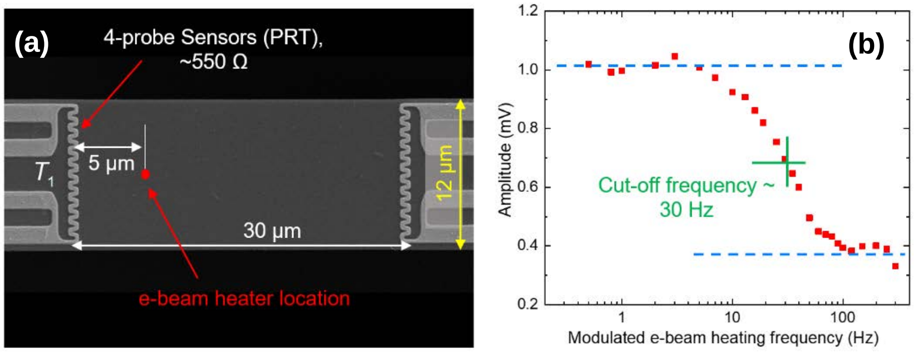

Figure 13. (a) E-beam from SEM is focused on the marked position with spot mode. (b) The PRT1 voltage amplitude induced by the modulated e-beam heating source.

DISTRIBUTION A: Distribution approved for public release.

However, due to the large signal noise at high frequency which is supposed to decay to minimum level, the cut-off frequency determination from this structure will not be able to determine any thermal properties. This is caused by the large thermal time-constant from this structure. By designing a similar structure with small span width will significantly reduce the thermal constant which can make this kind of measurement more practical.

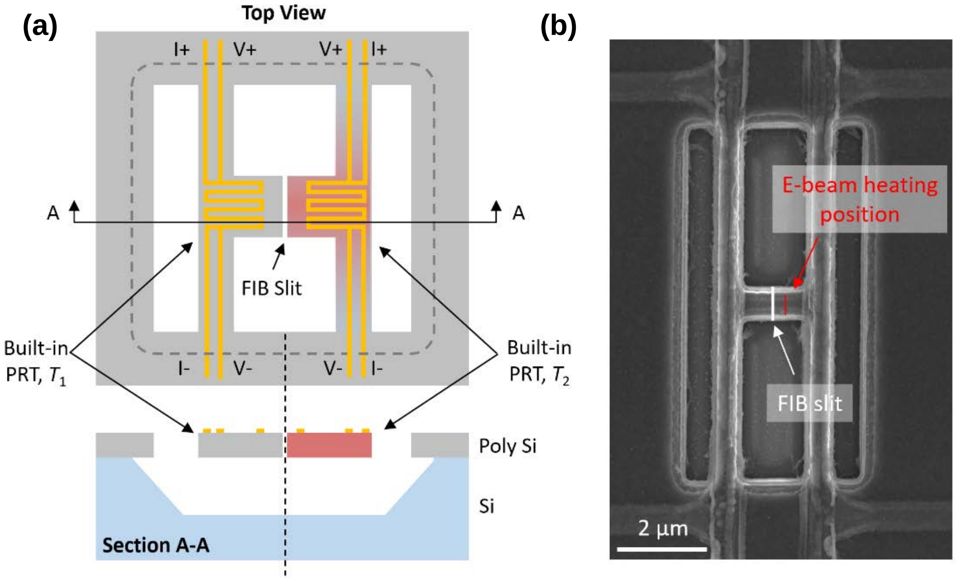

Figure 14. (a) The test structure to apply modulated e-beam heat source to measure the thermal properties of polysilicon. (b) The SEM image of the test structure.

As shown in Fig. 14, this is the test structure working principle, there are two symmetric polysilicon based structure. The built-in PRT will serve as the thermometer, the suspended structure will be modified by FIB (focused ion beam) to create a thermal bridge (cantilever like structure) with length less than 500 nm. By placing the e-beam heating position close to the edge of the FIB slit, the thermal constant can be estimated to be around 60 µs.[65] In this case, we can still monitor transient heat transfer (temperature rise) by modulating the e-beam up to 200 MHz. And this characterization of modulated e-beam will allow us to further apply e-beam to study non-diffusive thermal energy transport.

DISTRIBUTION A: Distribution approved for public release.

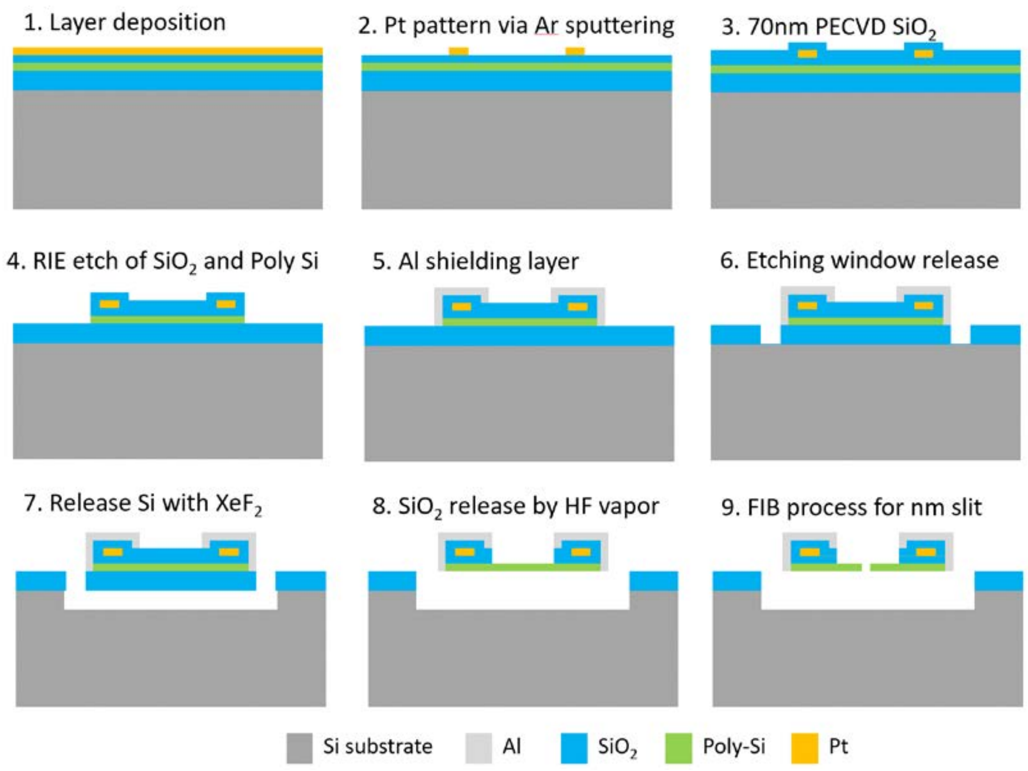

Figure 15. The nano-fabrication process for the modulated e-beam heating test structure.

D. Characterization of the thermal energy volumetric distribution from electron beam

The theoretical and experimental study of electron beam absorption can only give us the energy absorption ratio without any spatial information. As shown in Figure 2 (a), the e-beam heating is not exactly localized heating source, instead it generates a large interaction volume. However, for thin film, with larger voltage, the interaction within the thin film is much smaller which can provide ultra-small localized heating source that cannot be realized by laser. The information about the real interaction volume will be critical to apply e-beam as a nanoscale heat source or signal generation analysis.

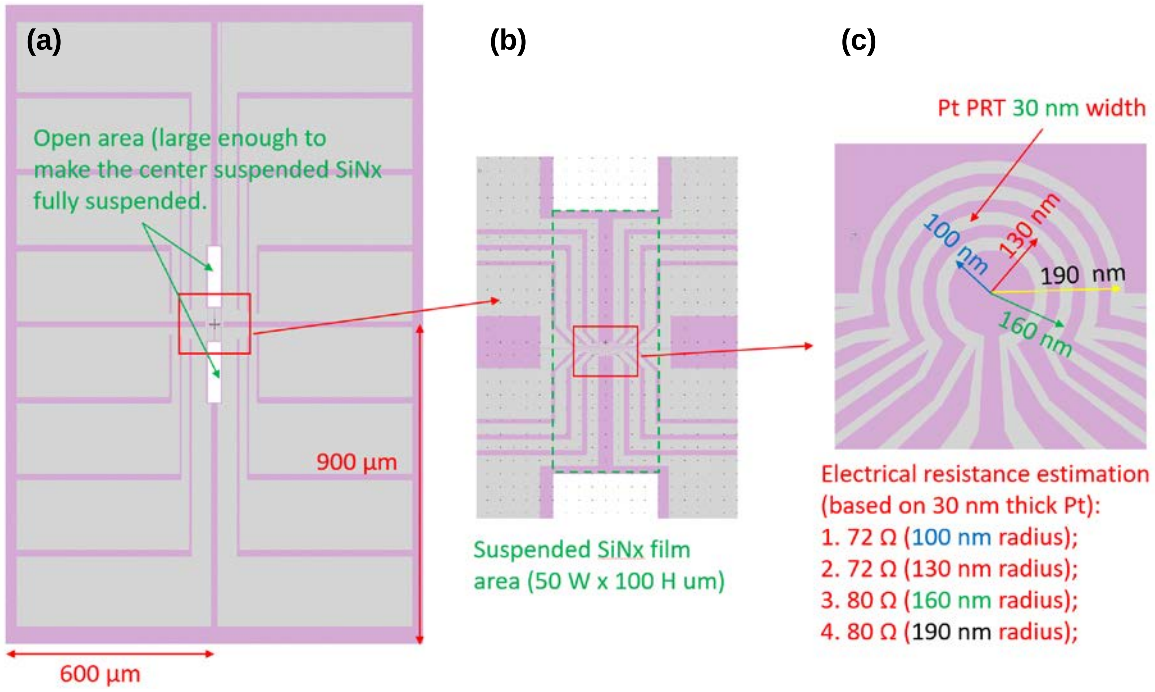

Figure 16. A circular test structure to study the volumetric thermal energy distribution inside of silicon nitride thin film induced by electron beam from SEM. (a) The design top view of the symmetric structure. (b) The enlarged structure of the center PRT design. (c) The PRT distribution, there are four circle PRT.

Figure 16 shows the test structure to study the volumetric thermal energy distribution inside of silicon nitride thin film induced by electron beam. Four homocentric circular PRTs can give the temperature information induced by the e-beam at the center. From this, we can determine the energy distribution of the absorbed thermal energy from e-beam interaction.

The device is designed as shown in Figure 16, and is still under fabrication at Center for Integrated Nanotechnologies of Los Alamos National Laboratory, Loa Alamos, NM.

E. Electron-beam based Time domain Pump-probe technique (ETPT) development

Over the past two decades, ultrafast laser based time-domain thermoreflectance (TDTR) has emerged and evolved as a reliable, powerful, and versatile technique to measure the thermal properties of a wide range of bulk and thin film materials and their interfaces. However, it still lack the spatial resolution to measure the temperature gradient or difference or the heat flux across a length scale below tens of micrometers due to the diffraction limit of laser light. Besides, TDTR measures thermal properties through the reflectance change with temperature, known as the thermoreflectance. Which means that the samples have to be coated with a thin metal film acting as transducer whose surface reflectance changes linearly with temperature when the temperature rise is small. The thermoreflectance technique was first developed in the 1970s and 1980s, where continuous wave (CW) light sources were used for the heating and sensing.[66] The TDTR method measures the thermoreflectance response as a function of delay time between the arrival of the pump and probe pulses on the sample surface (transducer surface), where the pump beam deposits a periodic heat flux on the sample surface and the probe beam detects the corresponding temperature change through the reflectance change. The reflected probe beam is collected by a fast-response photodiode detector (picked up by a lock-in amplifier), which converts the optical signals into electrical signals.

The proposed idea, e-beam pump-probe technique, applies e-beam from SEM as a heating source, and the temperature is detected by the secondary-electron signal generated from the electron-matter interaction.

As we know, the secondary electrons (SEs) is the most commonly used imaging mode in the SEM but has not previously been applied to measure temperature. However, several reports show that a small effects on SE yield in different materials. Typically, for most of materials tested, the SE emission was reported to decrease for a sample temperature rise yielding a temperature coefficient around -10^{4} K^{-1}. Several material parameters change with temperature which could plausibly contribute to a change in SE emission, such as the work function, electronic bandgap, and populations of phonons which can scatter SEs. Though the underling physics of this temperature dependent SE emission is still not clear, we can practically apply this phenomenon to develop the SEM thermometry which is the foundation of the e-beam pump-probe technique.

DISTRIBUTION A: Distribution approved for public release.

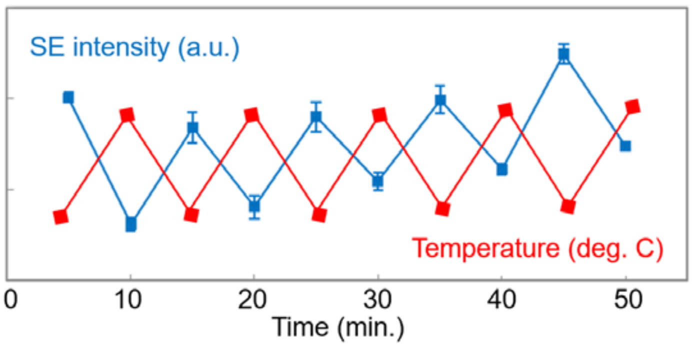

Figure 17. (Reproduced from JOURNAL OF APPLIED PHYSICS 124, 195104 (2018)) Typical results for an undoped Si sample. Temperature of the sample while being thermally cycled. Thermal response of SEM grayscale intensity using the built-in in-lens SE detector.[48]

As shown in Figure 17, results are from a typical test. An undoped Si sample was thermally cycled between 29 °C and 78 °C, for every temperature step ΔT of ±50 °C, which after averaging over four complete hot/cold cycles corresponds to a temperature response coefficient ~ −2080 ppm/K.[48] This provides a relative good sensitivity for SEM thermometry.

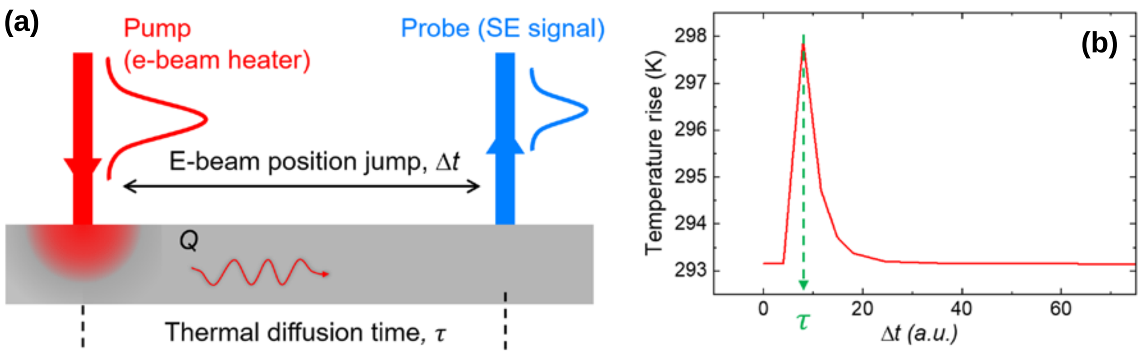

Figure 18. (a) The diagram of e-beam based pump probe technique. (b) The temperature signal extracted from the SE emission of probe location.

In the proposed e-beam based pump probe technique, a modulated e-beam will interact with the target sample to generate a thermal wave, then the e-beam will be shifted to another position to induce SE emission. The SE signal will be further processed to extract the local temperature information. From a thermal model considering the thermal diffusion between heating position and detection position, the thermal diffusivity of the sample can be directly determined.

The first proposed test structure will be a 400 µm long and 1.5 µm wide, 200 nm thick suspended structure. This is similar to the 1D strip device shown in Figure 8, but without the metal layer. Because the PRT based thermometer will be replaced by the SE thermometry. We marked the heating position at (-20 µm, 0), and sensing position at (20 µm, 0). For both heating and sensing, we have square wave pulsed e-beam energy input with different duty cycle as shown in Figure 18 (a). The initial e-beam heating power is set as 2 µW which can be determined from the results shown in Figure 7, the heating duration is set as 20 ms which will result in a temperature rise at sensing position (20 µm, 0) of 410 K. Then the e-beam with same power (2 µW, but duration is only 5 ms) will be shifted to sensing position with a time delay. With different delay time, the temperature at sensing position will be different and the decay curve of the initial e-beam heating can be fitted by determining the temperature at different delay time. For example, as shown in Figure 14, the temperature rise different of delay time of 2.5 ms and 15 ms will be around 45 K. The fitted temperature decay curve can be used to determine the thermal diffusivity of silicon nitride thin film which can share the thermal model from classic TDTR technique.

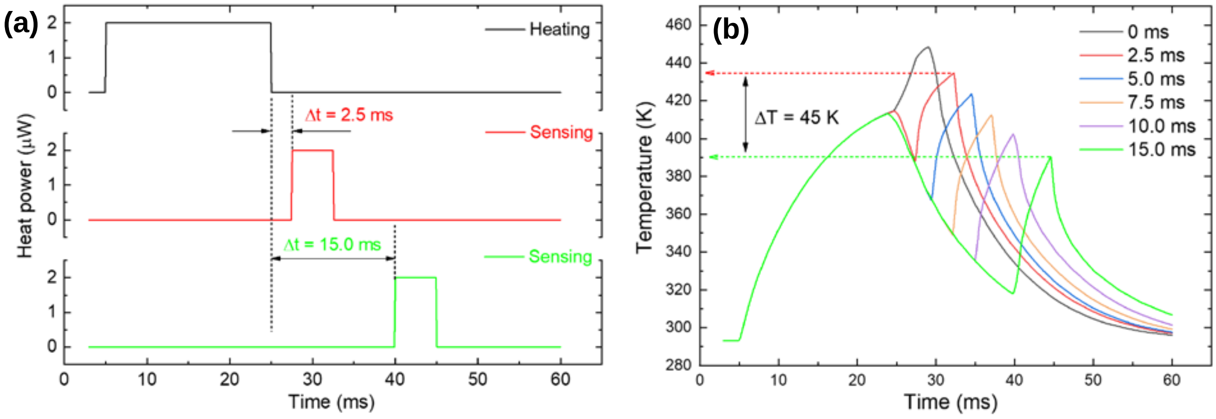

Figure 19. (a) The heating and sensing e-beam energy at different time. (b) The temperature information of sample at sensing position (20 µm, 0) which is a result of both initial heating and decayed sensing e-beam.

The e-beam position with time will be realized by a Python-based software platform (ScopeFoundry)[50]. Depend on the material and sample structure, the corresponding e-beam position with time function will be modified to derive the temperature decay curve the fit the thermal properties from this e-beam based pump-probe technique.

DISTRIBUTION A: Distribution approved for public release.

Some criteria have to be follow to develop or implement this technique:

1. The interested material's temperature dependent SE emission (in the unit of ppm/K) will have to be calibrated to determine the temperature rise at the sensing position of ETPT; while this will not the limit of this proposed technique, like TDTR, we can also deposit a transducer layer with standard material (with large SE emission sensitivity, means large absolute ppm/K).
2. To get the highest temperature rise to increase the sensitivity, a CASINO calculation can be used to determine the MEEHV.

Here we have to mention again, the greatest strength of the proposed ETPT can have great spatial resolution because that the e-beam can be focused to sub-nm scale to provide the related thermal probing technique with much higher resolution compared to laser based techniques.

Reference

1. Guo, H.; Khan, M.; Cheng, C.; Fan, W.; Dames, C.; Wu, J.; Minor, A. *Nature communications* **2014,** 5, 4986.

2. Lee, S.-Y.; Lee, W.-Y.; Thong, J. T.; Kim, G.-S.; Lee, S.-K. *Nanotechnology* **2016,** 27, (11), 115402.

3. Liu, D.; Xie, R.; Yang, N.; Li, B.; Thong, J. T. *Nano letters* **2014,** 14, (2), 806-812.

4. Zink, B.; Hellman, F. *Solid State Communications* **2004,** 129, (3), 199-204.

5. Queen, D.; Hellman, F. *Review of Scientific Instruments* **2009,** 80, (6), 063901.

6. Sultan, R.; Avery, A.; Stiehl, G.; Zink, B. *Journal of Applied Physics* **2009,** 105, (4), 043501.

7. Lee, S.-M.; Cahill, D. G. *Journal of Applied Physics* **1997,** 81, (6), 2590-2595.

8. Paddock, C. A.; Eesley, G. L. *Journal of Applied Physics* **1986,** 60, (1), 285-290.

9. Schmidt, A. J.; Cheaito, R.; Chiesa, M. *Review of Scientific Instruments* **2009,** 80, (9), 094901.

10. Pop, E. *Nano Research* **2010,** 3, (3), 147-169.

11. Grosse, K. L.; Bae, M.-H.; Lian, F.; Pop, E.; King, W. P. *Nature nanotechnology* **2011,** 6, (5), 287.

12. Chapuis, P.-O.; Greffet, J.-J.; Joulain, K.; Volz, S. *Nanotechnology* **2006,** 17, (12), 2978.

13. Egerton, R.; Li, P.; Malac, M. *Micron* **2004,** 35, (6), 399-409.

14. Groves, T. *Journal of Vacuum Science & Technology B: Microelectronics and Nanometer Structures Processing, Measurement, and Phenomena* **1996,** 14, (6), 3839-3844.

15. Leijten, Z. J.; Keizer, A. D.; de With, G.; Friedrich, H. *The Journal of Physical Chemistry C* **2017,** 121, (19), 10552-10561.

16. Liu, M.; Xu, L.; Lin, X. *Scanning* **1994,** 16, (1), 1-5.

17. Almasi, G.; Blair, J.; Ogilvie, R.; Schwartz, R. *Journal of Applied Physics* **1965,** 36, (6), 1848-1854.

18. Yasuda, M.; Kawata, H.; Murata, K.; Hashimoto, K.; Hirai, Y.; Nomura, N. *Journal of Vacuum Science & Technology B: Microelectronics and Nanometer Structures Processing, Measurement, and Phenomena* **1994,** 12, (3), 1362-1366.

19. Joy, D. C., *Monte Carlo modeling for electron microscopy and microanalysis*. Oxford University Press: 1995; Vol. 9.

20. Hovington, P.; Drouin, D.; Gauvin, R. *Scanning* **1997,** 19, (1), 1-14.

21. Drouin, D.; Hovington, P.; Gauvin, R. *Scanning* **1997,** 19, (1), 20-28.

22. Hovington, P.; Drouin, D.; Gauvin, R.; Joy, D. C.; Evans, N. *Scanning* **1997,** 19, (1), 29-35.

23. Movla, H.; Babazadeh, M. *Optik* **2014,** 125, (1), 71-74.

24. Tian, J.; Wu, J.; Chiu, Y.-L. *Ultramicroscopy* **2018,** 187, 13-19.

25. Wong, B. T.; Mengüç, M. P. *International Journal of Heat and Mass Transfer* **2009,** 52, (11-12), 2632-2645.

26. Wong, B. T.; Mengüç, M. P. *Journal of Quantitative Spectroscopy and Radiative Transfer* **2010,** 111, (3), 399-419.

27. Chu, D.; Bilir, D. T.; Pease, R. F. W.; Goodson, K. E. *Journal of Vacuum Science & Technology B: Microelectronics and Nanometer Structures Processing, Measurement, and Phenomena* **2002,** 20, (6), 3044-3046.

28. Chu, D.; Wong, W.-K.; Goodson, K. E.; Pease, R. F. W. *Journal of Vacuum Science & Technology B: Microelectronics and Nanometer Structures Processing, Measurement, and Phenomena* **2003,** 21, (6), 2985-2989.

29. Wang, Z.; Gui, L.; Han, D.; Xu, Z.; Han, L.; Xu, S. *Nanoscale research letters* **2019,** 14, (1), 31.

30. Wang, Z.; Yang, F.; Han, D.; Li, G.; Xu, J.; Xu, S. *Journal of Vacuum Science & Technology B, Nanotechnology and Microelectronics: Materials, Processing, Measurement, and Phenomena* **2017,** 35, (4), 041601.

31. Wang, Z.; Xie, R.; Bui, C. T.; Liu, D.; Ni, X.; Li, B.; Thong, J. T. *Nano letters* **2011,** 11, (1), 113-118.

32. Zhao, Y.; Zhang, G.; Nai, M. H.; Ding, G.; Li, D.; Liu, Y.; Hippalgaonkar, K.; Lim, C. T.; Chi, D.; Li, B. *Advanced Materials* **2018,** 30, (50), 1804928.

33. Aiyiti, A.; Bai, X.; Wu, J.; Xu, X.; Li, B. *Science Bulletin* **2018,** 63, (7), 452-458.

34. Lowney, J. R. *J. Microbeam Analysis* **1995,** 4, (J. Microbeam Analysis).

35. Czyżewski, Z.; MacCallum, D. O. N.; Romig, A.; Joy, D. C. *Journal of Applied Physics* **1990,** 68, (7), 3066-3072.

36. Prodanović, V.; Chan, H.; Graaf, H.; Sarro, P. *Nanotechnology* **2018,** 29, (15), 155703.

37. Bagolini, A.; Savoia, A. S.; Picciotto, A.; Boscardin, M.; Bellutti, P.; Lamberti, N.; Caliano, G. *Journal of Micromechanics and Microengineering* **2014,** 25, (1), 015012.

38. Niedrig, H. *Journal of Applied Physics* **1982,** 53, (4), R15-R49.

39. Neubert, G.; Rogaschewski, S. *Journal of Physics D: Applied Physics* **1984,** 17, (12), 2439.

40. Kanaya, K. a.; Okayama, S. *Journal of Physics D: Applied Physics* **1972,** 5, (1), 43.

41. Fitting, H. J. *physica status solidi (a)* **1974,** 26, (2), 525-535.

42. Lagos, M. J.; Reyes-Coronado, A.; Konečná, A.; Echenique, P. M.; Aizpurua, J.; Batson, P. E. *Physical review B* **2016,** 93, (20), 205440.

43. Yuehui, Y.; Xianghuai, L.; Ziwei, F.; Shichang, Z. *Applied surface science* **1989,** 40, (1-2), 145-150.

44. Shi, L.; Li, D.; Yu, C.; Jang, W.; Kim, D.; Yao, Z.; Kim, P.; Majumdar, A. *Journal of heat transfer* **2003,** 125, (5), 881-888.

45. Zheng, J.; Wingert, M. C.; Dechaumphai, E.; Chen, R. *Review of Scientific Instruments* **2013,** 84, (11), 114901.

46. Wu, J. Y.; Wu, W.; Pettes, M. T. *Review of Scientific Instruments* **2016,** 87, (9), 094901.

47. Lim, S.-J.; Lee, C.-H. In *Analysis of probe current in scanning electron microscopy*, 2008 International Conference on Control, Automation and Systems, 2008; IEEE: pp 1200-1203.

48. Khan, M.; Lubner, S.; Ogletree, D.; Dames, C. *Journal of Applied Physics* **2018,** 124, (19), 195104.

49. Dong, J.; Du, P.; Zhang, X. *Thin Solid Films* **2013,** 545, 414-418.

50. Durham, D. B.; Ogletree, D. F.; Barnard, E. S. *Surface and Interface Analysis* **2018,** 50, (11), 1174-1179.

51. Fuchs, K. In *The conductivity of thin metallic films according to the electron theory of metals*, Mathematical Proceedings of the Cambridge Philosophical Society, 1938; Cambridge University Press: pp 100-108.

52. Sondheimer, E. H. *Advances in physics* **1952,** 1, (1), 1-42.

53. Majumdar, A. **1993**.

54. Sultan, R.; Avery, A.; Underwood, J.; Mason, S.; Bassett, D.; Zink, B. *Physical Review B* **2013,** 87, (21), 214305.

55. Sikora, A.; Ftouni, H.; Richard, J.; Hébert, C.; Eon, D.; Omnes, F.; Bourgeois, O. *Review of Scientific Instruments* **2012,** 83, (5), 054902.

56. Wu, X.; Hull, R. *Nanotechnology* **2012,** 23, (46), 465707.

57. Wehmeyer, G.; Bustillo, K. C.; Minor, A. M.; Dames, C. *Applied Physics Letters* **2018,** 113, (25), 253101.

58. Idrobo, J. C.; Lupini, A. R.; Feng, T.; Unocic, R. R.; Walden, F. S.; Gardiner, D. S.; Lovejoy, T. C.; Dellby, N.; Pantelides, S. T.; Krivanek, O. L. *Physical review letters* **2018,** 120, (9), 095901.

59. Lagos, M. J.; Batson, P. E. *Nano letters* **2018,** 18, (7), 4556-4563.

60. He, L.; Hull, R. *Nanotechnology* **2012,** 23, (20), 205705.

61. Mecklenburg, M.; Hubbard, W. A.; White, E.; Dhall, R.; Cronin, S. B.; Aloni, S.; Regan, B. *Science* **2015,** 347, (6222), 629-632.

62. Zhang, X.; Grigoropoulos, C. P. *Review of Scientific Instruments* **1995,** 66, (2), 1115-1120.

63. Griffin Jr, A.; Brotzen, F.; Loos, P. *Journal of Applied Physics* **1994,** 76, (7), 4007-4011.

64. Zeng, L.; Collins, K. C.; Hu, Y.; Luckyanova, M. N.; Maznev, A. A.; Huberman, S.; Chiloyan, V.; Zhou, J.; Huang, X.; Nelson, K. A. *Scientific reports* **2015,** 5, 17131.

65. Gu, Y.-F.; Zhou, Z.-F.; Sun, C.; Li, W.-H.; Huang, Q.-A. *Micromachines* **2016,** 7, (10), 174.

66. Rosencwaig, A. *Science* **1982,** 218, (4569), 223-228.